Determining hydrodynamic forces in bursting bubbles using DNA nanotube mechanics

Rizal F. Hariadi[a], Erik Winfree[b], and Bernard Yurke[c,1]

[a]Applied Physics, California Institute of Technology, Pasadena, CA 91125; [b]Bioengineering, California Institute of Technology, Pasadena, CA 91125; and [c]Department of Materials Science and Engineering, Boise State University, Boise, ID 83725

Quantifying the mechanical forces produced by fluid flows within the ocean is critical to understanding the ocean's environmental phenomena. Such forces may have been instrumental in the origin of life by driving a primitive form of self-replication through fragmentation. Among the intense sources of hydrodynamic shear encountered in the ocean are breaking waves and the bursting bubbles produced by such waves. On a microscopic scale, one expects the surface-tension–driven flows produced during bubble rupture to exhibit particularly high velocity gradients due to the small size scales and masses involved. However, little work has examined the strength of shear flow rates in commonly encountered ocean conditions. By using DNA nanotubes as a novel fluid flow sensor, we investigate the elongational rates generated in bursting films within aqueous bubble foams using both laboratory buffer and ocean water. To characterize the elongational rate distribution associated with a bursting bubble, we introduce the concept of a fragmentation volume and measure its form as a function of elongational flow rate. We find that substantial volumes experience surprisingly large flow rates: during the bursting of a bubble having an air volume of 10 mm^3, elongational rates at least as large as $\dot{\epsilon} = 1.0 \times 10^8 \ s^{-1}$ are generated in a fragmentation volume of $\sim 2 \times 10^{-6} \ \mu L$. The determination of the elongational strain rate distribution is essential for assessing how effectively fluid motion within bursting bubbles at the ocean surface can shear microscopic particles and microorganisms, and could have driven the self-replication of a protobiont.

DNA nanotechnology | polymer dynamics | hydrodynamics

Functioning like a giant heat engine between the high-temperature heat bath of the sun and the low-temperature heat bath of outer space, the earth's atmosphere generates wind and rain with intense fluid flows. The mechanical stresses produced by these hydrodynamic flows are among the environmental stresses that biological organisms must cope with. Organisms often exploit these stresses and fluid flows, most notably to aid reproduction. A well-known example at the macroscopic scale is the wind dispersal of spores, seeds, and pollen. Less well-known, fragmentation resulting from fluid-flow-induced stress is used by a number of marine organisms as a means of vegetative reproduction, such as macrophyte algae (1) and sponge and coral colony (2, 3) propagation by storm-induced fragmentation. Can analogous mechanical forces facilitate vegetative reproduction at the microscale? Current evidence is at best indirect: Filamentous cyanobacteria are known to fragment under environmental stress (4, 5), suggesting that prokaryotes may use fluid-flow-induced fragmentation as a means of clonal reproduction and dispersal as well.

Several origin-of-life hypotheses invoke processes in which environmentally produced microscale mechanical forces drive self-replication through fragmentation. Oparin proposed that fragmentation of coacervates may have constituted a primitive form of self-replication allowing for Darwinian evolution by natural selection (6). More concretely, Cairns-Smith proposed that life arose from mineral crystals that replicated by fragmentation into new seed crystals, thereby propagating genetic information consisting of the patterns of defects within the mother crystal (7–9).

Szostak's group also proposed that division of protocells (having a lipid bilayer) can be driven by fluid flow (10–12). Inspired by Cairns-Smith's proposal, Schulman, Yurke, and Winfree used DNA tile self-assembly to construct a self-replicating system in which fragmentation was induced by intense elongational flow at a constriction in a flow channel (13). This synthetic system is analogous to an in vitro system in which exponential growth of prions is driven via fragmentation by mechanical shearing of amyloid fibrils (14). Similarities between regeneration (self-healing) and asexual reproduction in modern organisms have led some to postulate fragmentation-and-regeneration as a primordial form of reproduction (15).

To effectively shear microscopic objects such as bacteria or protobionts, fluid flows must exhibit high-velocity gradients over the length scale of the object. Such small-scale high-velocity-gradient flows occur naturally in breaking ocean waves that produce whitecaps (16). Within these waves, the highest velocity gradients are expected to occur in the films of bursting bubbles due to the rapid acceleration produced by surface tension forces acting on the small fluid mass. Moreover, bursting bubbles can generate mechanical stresses of sufficient intensity to be biologically relevant to organisms living in the sea surface microlayer (neuston) (17). As a technological example, cell death at the air–liquid interface during the sparging of bioreactors to enhance oxygen diffusion has been attributed to bubble bursting (18).

The fluid flows most effective at shearing small free-floating objects are those that exhibit strain deformation. In such flows, a rod-shaped object will tend to align itself along the direction of maximum fluid extension. In this orientation the rod experiences the greatest tensile stress and is most susceptible to fragmentation.

Significance

The hydrodynamic forces within bursting bubbles are of interest for their relevance to small-scale fluid mechanics, bioreactor efficiency, pollutant degradation, and the origin of life. However, despite the 150-year history of their study, the strengths of flows within bursting bubbles are only hypothetically known. Here, we show that DNA nanotubes—architecturally similar to biological microtubules—are fragmented during the bubble bursting process. Further, by analyzing the resulting fragment lengths, we characterize the spectrum of elongational flow rates, revealing that surprisingly strong tensile forces can be generated—in principle sufficient to fragment filamentous cyanobacterial chains, lipid vesicle protocells, genomic DNA, and other long polymeric molecules residing within or near the disintegrating liquid film.

In a given fluid element, the rate of fluid extension—i.e., the rate at which two points in the fluid separate, divided by the distance between them—has a maximum that is referred to as the elongational rate and is here denoted by $\dot{\epsilon}$. A useful way to conceptualize the meaning of $\dot{\epsilon}$ is to consider the case when it is constant. In this case, the time it takes for the fluid element to double its length is $t_b = \ln(2)/\dot{\epsilon}$.

Fig. 1 shows a mechanism by which rod-shaped objects within bursting fluid films can be fragmented. As the hole produced in the bubble film expands, its circumference increases (Fig. 1B). Due to this, fluid elements near the hole's edge will experience elongation in the direction perpendicular to the velocity of the hole edge. As shown in Fig. 1 C and D, rod-shaped structures within the bubble film will align along the circumference of the expanding hole. If the tension generated along the length of the structure exceeds its tensile strength, the structure will fragment (Fig. 1E).

The elongational rates generated by this mechanism can be estimated using a model of film hole dynamics, for a film of uniform thickness. Initially considered by Dupré (19), Rayleigh (20), and Ranz (21), then corrected by Culick (22) and Taylor (23), the model treats the rupture as a circular hole that propagates outward with the film fluid accumulating in a toroid at the hole perimeter. From momentum balance, the hole propagates outward with a constant speed $v = \sqrt{2\sigma/\rho\delta}$, where σ is the surface tension of the film, ρ is the fluid density, and δ is the film thickness. The elongational rate of the circumference is given by $\dot{\epsilon} = v/r$, where r is the hole radius. The volume of fluid subjected to elongational rates greater than $\dot{\epsilon}$, in this simple model, is given by $V_f(\dot{\epsilon}) = \pi\delta r^2 = 2\pi\sigma/\rho\dot{\epsilon}^2$, which is, surprisingly, independent of film thickness. Such volumes provide a natural way to characterize the ability of a bursting bubble to fragment objects suspended within the bubble film that will shear under given elongational rate $\dot{\epsilon}$. Importantly, $V_f(\dot{\epsilon})$ can be defined in a model-independent way as the volume of fluid that experiences elongational rates greater than $\dot{\epsilon}$ during the course of bubble bursting. We will refer to such volumes as fragmentation volumes.

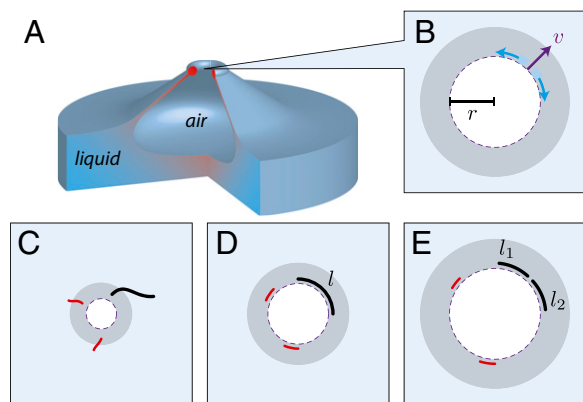Although easiest to explain, the Culick and Taylor model does not describe the only type of elongational flow that can be generated within a bursting bubble; therefore the estimate for $V_f(\dot{\epsilon})$ based on this model should be considered a loose lower bound for the true value. In fact, only half the surface-tension energy released is converted into the kinetic energy of the outward motion of the fluid (24). This suggests that the other half of the surface-tension energy must be dissipated within the film near the edge of the hole. For fluids with low viscosity, such as water, this implies that there are intense small-scale fluid flows near the edge of the hole (18) in addition to those illustrated in Fig. 1. Hydrodynamic instabilities, particularly with larger bubbles, can occur along the perimeter, resulting in fingering and the formation of droplets (25). Also, particularly for small bubbles, the expanding hole produces an inward propagating wave at the bottom surface of the bubble that forms a jet that may launch droplets (26, 27). High-flow gradients are expected in the region where these jets pinch to form droplets. A recent discussion of droplet production during bubble bursting in ocean-like (i.e., not soapy) water was given by Lhuissier and Villermaux (28).

As discussed by Lhuissier and Villermaux, at the instant the bubble bursts it possesses a cap of uniform thickness that, at a well-defined edge, joins with the bulk fluid in a region where the thickness rapidly increases with distance from the center of the bubble (Fig. 1A). The critical thickness at which bubble films spontaneously burst depends on the bubble radius (28), increasing from 0.05 to 30 μm as the bubble radius increases from 1 to 20 mm. For an object such as a microorganism to be fully impacted by the mechanical stresses produced by bubble bursting, it would have to reside in the cap film or close to the cap boundary; that is, its thinnest dimension would have to be smaller than the film thickness. Nevertheless, mechanical stresses produced by bursting bubbles are among the stresses that microorganisms, particularly those that occupy the niche consisting of the neuston or sea surface microlayer (29–31), must cope with. We hypothesize that protobionts, small enough to be suspended within the bubble film, also occupied this niche and used these stresses to facilitate replication. However, little work seems to have been done to characterize the elongational rates produced during the bursting of a bubble that would facilitate assessing whether forces of sufficient magnitude are generated.

In this study the fragmentation of DNA nanotubes is used to characterize both the magnitude of the elongational rates produced and the volume of fluid subjected to these elongational rates during bubble bursting. These nanotubes are constructed from short DNA oligomers referred to as single-stranded tiles, which each have four sequence domains by which a given oligomer binds with four neighboring oligomers via Watson–Crick base pairing. Thus, whereas each DNA oligomer is held together by covalent bonds, the entire tube assembly is held together by the supramolecular interactions that enable two complementary single-stranded oligomers to form duplex DNA. Base sequences of the oligomers are designed so that the axes of the duplex DNA are parallel to the long axis of the tube. The supramolecular Watson–Crick bonds between neighboring single-stranded tiles are much weaker than the covalent bonds of the phosphate backbone of a single-stranded tile (32). Under sudden tension along the axis of the duplex DNA (33), the tensile force at which the supramolecular bonding fails is referred to as the overstretching force f_c, which has a value of about 65 pN (34, 35). For a tube in which there are n duplex strands in cross-section, the tensile force will be $T_c = nf_c$. For the tubes used in the experiments reported here, $n = 7$ (*SI Appendix*, Fig. S1) and consequently the tubes fragment when subjected to tensile forces in excess of 455 pN. The tubes have a radius of 4 nm, a persistence length of 5 μm (36), and a length distribution that peaks at 5 μm at the start of the experiment (*SI Appendix*, Fig. S2; see Fig. 3 B and G).

Some of these tubes will be trapped in the bubble film and will be subjected to elongational forces in the manner illustrated in Fig. 1. Although nanotubes will necessarily also be subject to

Fig. 1. DNA nanotubes fragmentation by bursting bubbles. Side (A) and top (B) views of a bubble filled with air bursting on a water surface. Color gradient loosely corresponds to the expected magnitude of the hydrodynamic forces. (B–E) As the hole travels outward driven by surface tension, the liquid film is accumulated into a growing toroidal rim (gray rings). The enlargement of the hole produces elongational flow, with rate $\dot{\epsilon} = v/r$, which is tangential to the perimeter where r is the hole radius and v is the outward velocity of the hole perimeter. The two blue arcs are the two volume elements of the bursting film. (C and D). As the hole expands, the fluid flow orients DNA nanotubes (black, red). (D and E) The elongational flow breaks sufficiently long DNA nanotubes (black) of length l into fragments of length l_1 and l_2 due to tension applied to the nanotube by the elongational fluid flow. Short nanotubes (red) are not fragmented due to insufficient build-up of tension.

compressive fluid flows, they are not fragile under compression. The junctions at which a given single-stranded tile connects with two neighboring tiles are flexible, allowing the tube to crumple and then straighten when the compressive forces are relieved. This collapse into a coil configuration followed by stretching has been studied for other stiff linear biopolymers and synthetic fibers in hydrodynamic flows near stagnation points (33, 37, 38). Generally, the tubes will crumple under the compressive flow and reorient and stretch along the axis of the elongational flow (Movie S1 and *SI Appendix*, section 10). A further complication is that Brownian motion will tend to counteract the alignment produced by the elongational flow. However, as will be shown, under the conditions in which our DNA nanotubes break, the Péclet number—which is the ratio of the active transport rate to the diffusive transport rate— is in excess of 1.4×10^4, indicating that diffusive misalignment of the nanotubes plays a negligible role in our experiments. Due to the viscous stresses exerted on the DNA nanotube as it reorients along the direction of maximum extension flow, the tension experienced by the tube will be greatest at the center of the tube and will be greater for longer tubes, scaling as $T \propto \dot{\epsilon} l^2 / \ln(l/2R)$, where l is the tube length and R the tube radius (34). If the tensile force is exceeded, the tube will break into two fragments of nearly equal length. If the elongational flow continues to intensify so that the two fragments experience a tension at their centers that exceeds the tensile force, each of these in turn will fragment into two shorter pieces of equal length. This cascading process will continue until the elongational rate reaches its maximum value.

DNA nanotubes are well-suited to serve as probes of hydrodynamic flows within bubble films for three reasons. First, their fragmentation in elongational flows has already been extensively characterized (34). Second, they are highly soluble in water and do not exhibit a surfactant-like tendency to stick to the air–water interface, unlike many proteins. Third, it is straightforward to measure histograms of nanotube lengths using fluorescence microscopy. Here, from the evolution of the DNA nanotube fragment length during the course of bubbling, we were able to determine the fragmentation volumes for elongational rates over five orders of magnitude, although our experimental techniques were not able to distinguish where the DNA nanotubes were broken within the bubble. Our findings suggest that, via bubbles, ocean waves provide a source of strong mechanical forces at the micron-scale mechanical stresses that ocean surface-dwelling microbes must cope with, that may be involved in the natural breakdown of pollutants, and that would have been available for protobionts to use as a means of driving self-replication.

Results

Fig. 2 shows the experimental setup and molecular design.

DNA Nanotubes. For the experiments, DNA nanotubes with monodisperse diameter and bond strength were used (32, 34). These tubes were self-assembled from 7 DNA oligomers (Fig. 2D and *SI Appendix*, Fig. S1), as described in *Materials and Methods*. The tubes seldom grow longer than 20 μm and have a persistence length of over 5 μm (36), making them more amenable to theoretical analysis than a reptating polymer. For the experiments here, they can be regarded as rigid rods that break when an axial tensile force of 455 pN is applied (34).

Bubble Production at Constant Rate and Precise Bubble Size. Bubbles were generated by flowing air through buffer solution containing DNA nanotubes (Fig. 2). Air was supplied via a motorized syringe pump equipped with a 60-mL syringe [26.70-mm inner diameter (ID)]. To minimize evaporation, the air was delivered via polyethylene tubing, 0.58-mm ID, and was bubbled through a humidifier consisting of a 15-mL centrifuge tube filled to 13.5 mL with the assay buffer [1× TAE (40 mM Tris-acetate and 1 mM EDTA) with 12.5 mM $MgCl_2$]. Two stainless steel capillaries,
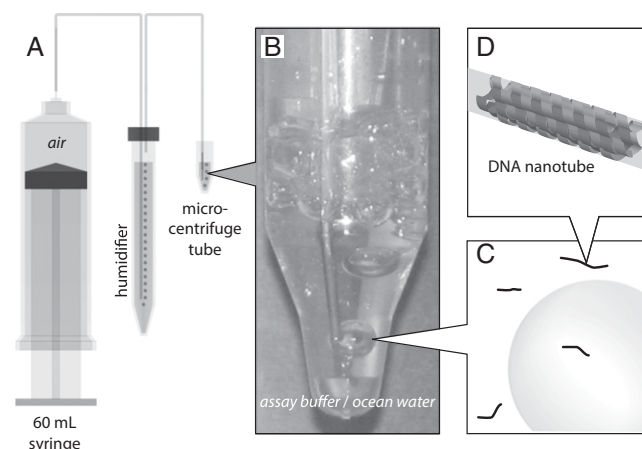

Fig. 2. Bubbles production apparatus. (A) Schematic of apparatus. (B) Sample, housed in a microcentrifuge tube, to which air is being delivered. For scale, the OD of the upper section of the microcentrifuge tube is 1.1 cm. (C) Bubbles and 7-helix nanotubes (not to scale) are in the solution. (D) Schematic of the 7-helix nanotube used in this experiment (*SI Appendix*, Fig. S1 and Table S1).

passing through the cap and cemented with silicone aquarium sealant, served as feedthroughs for air to and from the airtight humidifier chamber. The bubbles were generated at the end of a stainless steel capillary, 0.635-mm outer diameter (OD) and 0.432-mm ID, connected to the end of the polyethylene tubing that was pointed downward into the sample fluid (Fig. 2B). To minimize the amount of synthetic DNA used, the sample, typically consisting of 100 μL of fluid, was housed in a 2.0-mL microcentrifuge tube (Fig. 2B). The nose of the tube has a 4-mm ID and a depth of 6 mm. The tapered region flares out to a 1-cm ID.

Bubbles of different size were obtained by varying the airflow rate. Two airflow rates, 1.8 and 18 mL/min, were used in the experiments. A bubble volume V_b of 5.32 mm^3 at the slower airflow rate (1.8 mL/min) was determined from photographs of bubble production at the end of the capillary tube in a flat-walled flask containing assay buffer. The height and width of the bubbles were measured and the volumes were computed under the assumption that the bubbles are oblate spheroids. At the slower flow rate, individual bubbles reached the surface and burst before the arrival of subsequent bubbles. Larger bubbles were produced at the higher flow rate. By counting the number of bubbles produced over a known time interval at a given airflow rate, the ratio of the volume of the bubbles produced at 18 and 1.8 mL/min was measured to be 1.74 ± 0.26. From this ratio, a bubble volume V_b of 9.26 mm^3 was inferred for the higher flow rate (18 mL/min). At this bubbling rate, the sample chamber contained multiple bubbles at any one time, i.e., a foam, as shown in Fig. 2B. A mean bubble lifetime of ∼2 s was determined for both buffer and ocean water based on an estimate of the number of bubbles in the sample chamber divided by the rate of bubble production. This lifetime is intermediary between that of pure (distilled) water and saturated soap bubbles, indicating the presence of surfactant in highly dilute amounts, typical of tap water or water found in nature, such as river water, ocean water, and rain puddles (28). Due to drainage, bubble lifetime is related to the film thickness at bursting; for similar-sized bubbles bursting individually in tap water, Lhuissier and Villermaux (28) report thickness on the order of 100 nm.

Bubble Bursting Driven Fragmentation of DNA Nanotubes in Assay Buffer or in Ocean Water. To follow the fragmentation of the DNA nanotubes by bubbling, two experiments were performed in assay buffer and in ocean water at the 18-mL/min airflow rate. For the experiment in ocean water, a control sample was left undisturbed to assess the stability of the DNA nanotubes in ocean water

(*SI Appendix*, Fig. S3 *A* and *B*). At the beginning of the run, the mean fragment length of the DNA nanotube control sample was determined to be 7.01 ± 0.41 μm. At the end of 1 h, the mean fragment length in the undisturbed sample was measured to be 6.88 ± 0.42 μm, which is statistically indistinguishable from the initial value.

The experiment in assay buffer consisted of two runs. In the first run, 1-μL volumes were drawn at time points when $V_a = 0$, 60, and 240 mL of air had passed through the sample. In the second run, the data were acquired at $V_a = 0$, 9, 18, 36, 72, 180, and 360 mL. Representative total internal reflection fluorescence (TIRF) microscopy images taken from the second run samples are shown in Fig. 3 *A*, *C*, and *E* along with the corresponding length histograms (Fig. 3 *B*, *D*, and *F*). The data of both runs were treated as a homogeneous set (*SI Appendix*, Fig. S2). For the experiment in ocean water, samples were withdrawn at $V_a = 0$, 60, 120, and 360 mL (Fig. 3 *G–I* and *SI Appendix*, Fig. S3).

The evolution of DNA nanotube length distributions was quantified by measuring individual nanotube lengths in fluorescence images (34). DNA nanotubes were covalently labeled with Cy3 fluorophores at uniform density (1 Cy3 every 7 nm, *SI Appendix*, Fig. S1). As a consequence, the relation between emitted photons and fragment length is expected to be linear. By measuring the photons emitted by each nanotube and the contour length of the longest nanotube in each image, the length of each nanotube can be inferred directly from the photon counts, even for nanotubes whose length is less than the diffraction-limited resolution of the microscope (*Materials and Methods*).

The length distributions (Fig. 3 and *SI Appendix*, Figs. S2 and S3) show a decrease in mean fragment length $\langle l \rangle$ with increasing bubble bursting. After 20 min, when 360 mL of air had been bubbled through the sample, the mean fragment length was measured to be 1.04 ± 0.07 μm and 1.02 ± 0.10 μm for the experiments in assay buffer and ocean water, respectively. The decrease in mean fragment length showed that a substantial amount of tube fragmentation had occurred. Moreover, the assay buffer and ocean water histograms indicated that DNA nanotube fragmentation proceeds similarly in the two fluids.

Under shearing, the sum of tube lengths l_t should remain conserved. This was tested by measuring the total tube length per image for the samples extracted during the run in assay buffer at different time points. Fig. 4*A* shows that l_t remains constant as a function of the air volume that has passed through the sample, V_a. Because $l_t = N \langle l \rangle$, where N is the total number of nanotubes and $\langle l \rangle$ is the mean tube length, the time independence of l_t allows one to infer the population ratio $P_g = N/N_0$, where N_0 is the initial number of nanotubes, via $P_g = \langle l \rangle_0 / \langle l \rangle$, where $\langle l \rangle_0$ is the initial mean tube length. P_g, inferred by this method, is plotted as a function of V_a in Fig. 4*B*. There is a sevenfold increase in the number of nanotubes by the time an air volume of 360 mL has passed through the sample. The curves are the result of a global best fit of the theory presented in the *Model for Extracting the Fragmentation Volume* section to the experimentally measured tube length distributions.

To determine the smallest tube fragments that were produced, the concentration of tubes $c(l,t)$ in the length range $0 < l < \Delta_{bin}$ for $\Delta_{bin} = 1$, 1/2, 1/4, 1/8, 1/16, and 1/32 μm was tabulated at different V_a. In Fig. 4*C*, we plotted $c(0 < l < \Delta_{bin}, t)/\Delta_{bin}$, which is the observed nanotube concentration normalized to the bin of size Δ_{bin}. For $\Delta_{bin} \geq 1/16$ μm and larger, this quantity grows substantially with V_a, whereas for $\Delta_{bin} = 1/32$ μm the data remain relatively fixed, indicating that fragments as short as $1/16$ μm are produced. A comparison of the curves of Fig. 4*C* with that of the results of a global best fit of the theory presented in the model section to the experimentally measured tube length distributions is given in *SI Appendix*, Fig. S7.

In previously reported experiments (34), we have shown that the suddenly applied fluid elongational rate $\dot{\epsilon}$ required for midpoint scission of an initial nanotube of length l to produce two fragments that have identical length of $l/2$ is

$$\dot{\epsilon}(l) = \frac{4T_c \ln(l/2R)}{\pi \eta l^2}, \quad [1]$$

where R is the tube radius, η is the viscosity of the fluid, and the tension T_c required to break the tube is given by $T_c = nf_c$, where n
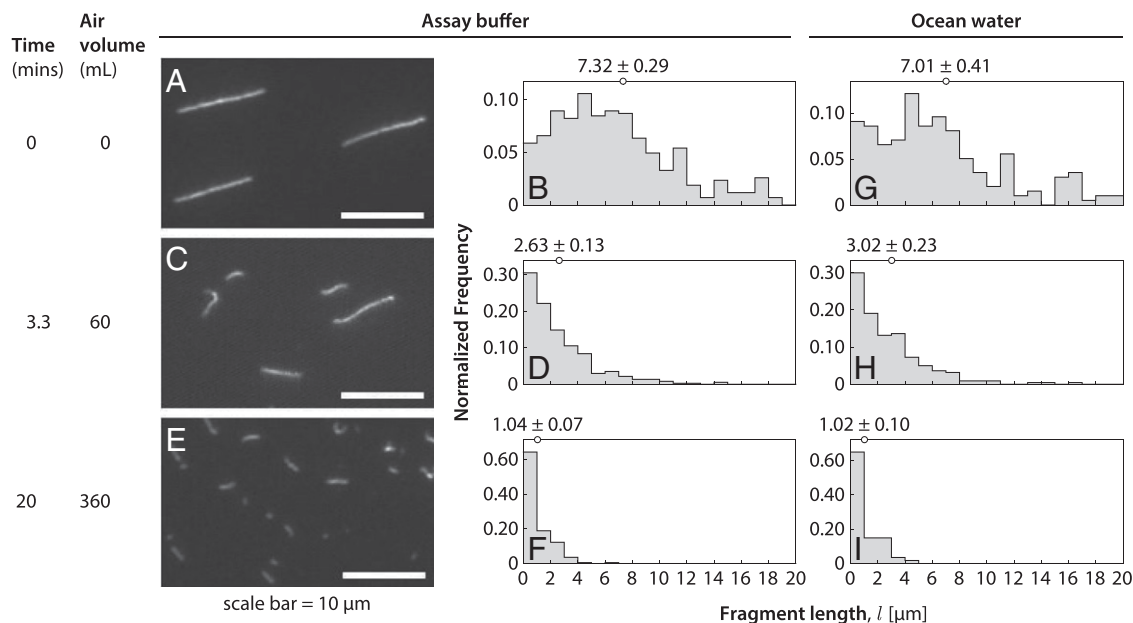

Fig. 3. Nanotube length distributions for bubble bursting experiments in assay buffer or in ocean water. Fluorescence microscopy images and fragment length distributions of DNA nanotubes withdrawn from a sample with an initial volume of 100 μL after 0 mL (*A* and *B*), 60 mL (*C* and *D*), and 360 mL (*E* and *F*) of air had passed through the sample at a flow rate of 18 mL/min. The mean tube length $\langle l \rangle$ for each distribution is given at the top of each histogram. Nanotube length distribution in bubble bursting experiment with ocean water after 0 mL (*G*), 60 mL (*H*), and 360 mL (*I*) of air.
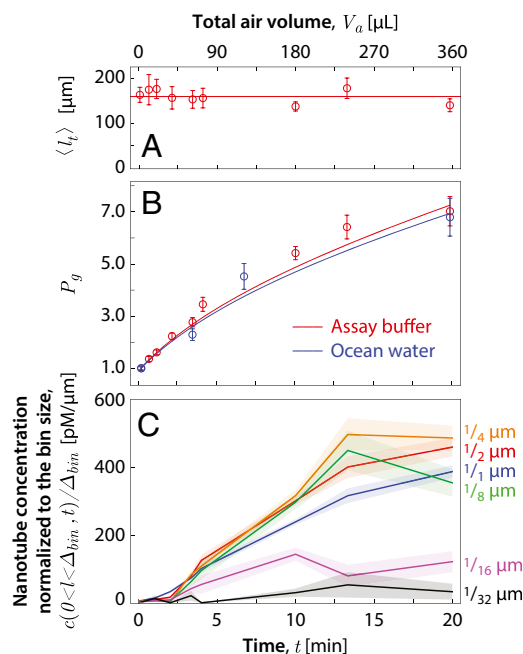
Fig. 4. DNA-nanotube fragmentation data as a function of the bubbling exposure time at a flow rate of 18 mL/min. (*A*) Total tube length per microscope field of view. The horizontal line represents a constant total tube length of 159 μm per image. Error bars show the SEM. (*B*) Plot of the population ratio P_g for experiments in assay buffer (red) and in ocean water (blue). The lines are the Bayesian fit to the experiments in assay buffer (red) and in ocean water (blue) based on the theory described in the model section. (*C*) Plot of the nanotube concentration per tube length $c(l, t)/\Delta_{bin}$ in the length range $0 < l < \Delta_{bin}$ for $\Delta_{bin} = 1, 1/2, 1/4, 1/8, 1/16$, and $1/32$ μm. (See *SI Appendix*, Fig. S2 for detailed histograms.)

is the number of duplex DNA strands along the circumference of the tube (*SI Appendix*, Fig. S1) and $f_c = 65$ pN is the critical force to overstretch a DNA helix (35). Note that the tension required to break the tube does not depend on the length of the duplex DNA segments that link successive tiles along the tube axis. This is because when stress is applied on a time scale that is short compared with that over which base pairs disassociate due to Brownian fluctuations, the strain will distribute uniformly along the linker duplex segments. All base pairs will break at once when this strain reaches the value where overstretching occurs. For our tubes, $n = 7$ and $R \approx 4$ nm. The observation of 1/16-μm tube fragments implies that tubes as short as 1/8 μm are broken in two via the hydrodynamic flows generated within the bubbles of the experiment of Figs. 3 and 4. Taking $\eta = 1.0 \times 10^{-3}$ Pa·s, Eq. **1** indicates that elongational flow rates at least as large as $\dot{\epsilon} = 1.0 \times 10^8$ s^{-1} are generated during bubble rupture.

Fragmentation Is Little Affected by the Bubble Production Rate. To show that fluid flow associated with bubble inflation and transport was not primarily responsible for the tube fragmentation, we repeated the experiment in assay buffer at an order of magnitude slower flow rate of 1.8 mL/min (*SI Appendix*, Fig. S4). The mean tube length when 60 mL of air had passed through the sample was 2.32 ± 0.13 μm. If, as presumed by our simple theoretical estimate based on film hole dynamics, a fixed amount of fragmentation occurs each time a bubble bursts, then the same amount of fragmentation should be apparent in samples that experienced the same number of bubbles. Because of the different size bubbles at the two flow rates, 60 mL of air at the slower flow rate generates the same number of bubbles as 104 mL of air at the faster flow rate. Interpolating between measured values for the faster flow rate of 18 mL/min (Fig. 3 and *SI Appendix*, Fig. S2)

yields a mean fragment length of 1.88 μm. This is only 20% shorter than found at the slower airflow rate, despite the 10-fold faster airflow rate, supporting a dominant role for bubble bursting rather than other hydrodynamic flows in the observed fragmentation processes. Furthermore, the similar degree of fragmentation in bubbles bursting individually at the surface (as for the slower flow rate) or in the context of a foam (as for the higher flow rate) suggests that the relevant hydrodynamic effects are similar for these two contexts.

Eliminating Bubble Bursting on the Water–Air Interface Suppresses Fragmentation. The assumption that fluid flows associated with bubble bursting are primarily responsible for tube breakage was confirmed by the suppression of tube fragmentation through the addition of 200 μL of heptane to the sample vial to form a fluid layer on top of the assay buffer. Air bubbles rising through this layer would leave the hydrophilic DNA in the aqueous phase. The aqueous fluid flows associated with this process are also reduced because of viscous coupling of the buffer with the heptane at the interface (39–41). The mean tube length when 60 mL of air was bubbled through the sample at 18 mL/min was 6.03 ± 0.50 μm (*SI Appendix*, Fig. S5), which is similar to the initial mean tube length 7.32 ± 0.29 μm and large compared with the mean tube length 2.63 ± 0.13 μm measured at $V_a = 60$ mL for the experiment of Fig. 3 and *SI Appendix*, Fig. S2.

Decreasing Surface Tension also Suppresses Fragmentation. Finally, we demonstrated that fluid flows associated with bubble bursting are primarily responsible for tube breakage by reducing tube fragmentation through the addition of 2 mM of the surfactant SDS to the assay buffer. The surfactant reduces the surface tension, increases surface viscosity effects (42), and increases the bubble lifetime. These effects inhibit nanotube breakage by reducing surface-tension–driven flow velocities and by reducing the film fluid volume through film drainage. The foam produced during this experiment necessitated using a 300-μL sample volume. Even then it was necessary to periodically stop the airflow to allow the foam to subside. Because of the 3× greater volume, the mean tube length $\langle l \rangle = 6.23 \pm 0.5$ μm at $V_a = 180$ mL for this experiment (*SI Appendix*, Fig. S6) should be compared with the $\langle l \rangle = 2.63 \pm 0.13$ μm at $V_a = 60$ mL for the experiment of Fig. 3 and *SI Appendix*, Fig. S2. Reducing the surface tension suppresses the breakage of the nanotubes. In agreement with previously published reports (43, 44), we verified that DNA nanotubes are stable in SDS buffer by constructing a length histogram of a control sample that was incubated in SDS buffer for 30 min without airflow. The final mean tube length 7.45 ± 0.54 μm was found to be statistically indistinguishable from the initial mean tube length 7.65 ± 0.58 μm, indicating the stability of DNA nanotubes in SDS buffer (*SI Appendix*, Fig. S6).

Model for Extracting the Fragmentation Volume. The results we have presented show that bursting bubbles will fragment DNA nanotubes and document how the fragment distribution in a fixed volume of fluid changes as a function of time as the fluid is cycled through the bursting bubbles. To apply these results more generally, one would like to know the number N of objects of a particular type that would be broken in a bubble if they are present in the fluid at concentration c and if an elongational rate of $\dot{\epsilon}$ was required to break them. The proportionality factor between N and c is the fragmentation volume $V_f(\dot{\epsilon})$; that is, $N = V_f(\dot{\epsilon})c$. The fragmentation volume is the sum of all of the fluid volume elements whose elongational rate has exceeded $\dot{\epsilon}$ at some point during the bubble rupture process. The fragmentation volume characterizes the fragmentation process for a single pass through a bubble. However, during the course of our experiments, a given nanotube or its fragments will have passed through bubbles multiple

times. This complicates the determination of $V_f(\dot{\epsilon})$ from the data. We will now describe how the time evolution of the DNA nanotube length distribution can be processed to extract $V_f(\dot{\epsilon})$.

Let $c(l,t)$ denote the concentration distribution of tubes of length l as a function of time t, such that in the limit $\Delta l \rightarrow 0$, $c(l,t)\Delta l$ is the concentration of tubes having lengths in the interval from $l - \Delta l/2$ to $l + \Delta l/2$ at a given time. The time evolution of the experimentally determined $c(l,t)$ contains information on how effectively a bubble can break a tube of length l. To extract the fragmentation volume from these data, a model is crafted for the case where the bubbles all have the same volume V_b, are produced a constant rate γ, and the sample volume V_s remains sufficiently well mixed that $c(l,t)$ can be regarded as constant over the sample volume. For the experiments reported here, $c(l,t)$ is expected to be uniform because the sample volume is small and well mixed by the fluid motion produced as the bubbles rise to the surface.

Let $r_f(l)$ be the rate with which tubes of length l are fragmented upon bursting of a bubble and let $r_b(l,l')$ be the rate per unit tube length that tubes of length l are produced from tubes of length l' upon bursting of a bubble. Then, the rate of change of $c(l,t)$ is given by

$$\frac{dc(l,t)}{dt} = -\gamma r_f(l)c(l,t) + \gamma \int_0^\infty r_b(l,l')c(l',t)dl', \quad [2]$$

where γ is the rate at which bubbles are produced (i.e., $\dot{V}_a/V_b$). Note that the lower limit of integration could have been set to l because $r_b(l,l') = 0$ for $l > l'$ because producing a new fragment of length l requires breakage of a tube longer than l. Because the total tube length per unit volume remains constant as the tubes are broken into shorter sections, one must have

$$\int_0^\infty lr_f(l)c(l,t)dl = \int_0^\infty l\int_0^\infty r_b(l,l')c(l',t)dl'dl. \quad [3]$$

The rate $r_f(l)$ is inversely proportional to V_s because this determines the frequency with which a given tube of length l will be within the vicinity of a bursting bubble. We thus write

$$r_f(l) = \frac{V_f(l)}{V_s}, \quad [4]$$

where the fragmentation volume $V_f(l)$ characterizes the effectiveness with which a bursting bubble breaks a tube of length l. Here, $V_f(l)$ is used as shorthand for $V_f(\dot{\epsilon}(l))$, where $\dot{\epsilon}(l)$ indicates the minimum elongational rate required to break tubes of length l. Similarly, we write

$$r_b(l,l') = n(l,l')\frac{V_f(l')}{V_s}, \quad [5]$$

where $n(l,l')$ is the mean number of tubes of length l per unit tube length produced by the fragmentation of a tube of length l'.

In principle, the functions $V_f(l)$ and $n(l,l')$ could be obtained through numerical calculation of the hydrodynamic flows of bursting bubbles and numerical calculation of the breakage of tubes within these hydrodynamic flows. To our knowledge, the requisite hydrodynamical calculations to determine $V_f(l)$ and $n(l,l')$ have not been carried out. The aim of the analysis here is to determine $V_f(l)$ using a plausible model for $n(l,l')$ in conjunction with our experimental data.

Imagine a small tube in the vicinity of a bubble that has begun to burst. The elongational flow rate of the fluid element the tube is imbedded in will increase over time. When the tension at the center

of the tube exceeds the tensile strength of the tube, the tube will break into two fragments of equal length. If the elongational rate continues to increase so that the tension at the center of the two shorter tubes exceeds the tube tensile strength, then again each of these two shorter tubes will break into two smaller tubes of equal length. At long times the fluid motions produced by the bursting bubble will dissipate, the bifurcation cascade will terminate, and the elongational flow rates within the fluid element containing the tube fragments will return to zero. One thus expects the fragmentation process to be a cascade of bifurcations. In the model for this case, which we call the "full cascade model," $n(l,l')$ is given by

$$n(l,l') = \sum_{m=1}^\infty 2^m p_m(l')\delta(l - l'/2^m), \quad [6]$$

where $p_m(l)$ is the conditional probability that a tube of length l has broken into 2^m fragments given that it has broken, the delta function ensures that $l' = 2^m l$, and the multiplier in front of the delta function is the number of fragments produced by a cascade of m bifurcations.

This is, of course, an idealization. Because of microscopic disorder, tubes are not expected to break exactly in half. However, our experience in modeling imperfections in tube breakage by hydrodynamic flows in another context indicates that the results are insensitive to the inclusion of such disorder in the modeling (34). More seriously, the assumption that the tube lengths are small compared with the length scale over which the elongational flow rate varies is likely to be violated in our experiments. Our longest tubes exceed 20 μm, which is likely to be substantially greater than the bubble film thickness. In this case, we expect a long tube to fragment into tubes having a distribution of lengths rather than into 2^m tubes of equal length. As an extreme case one might imagine that the tubes only break in two. This choice results in the "single bifurcation model," which uses

$$n(l,l') = 2\delta(l - l'/2). \quad [7]$$

We show in *SI Appendix*, Figs. S7–S9 and sections 3–6 that the single bifurcation model does not fit the data as well as the full cascade model. This indicates that the $c(l,t)$ data have the power to distinguish between models of $n(l,l')$ and suggests that Eq. **6** is a satisfactory approximation for our experiments.

As shown in *SI Appendix*, section 3, Eq. **2**, using Eqs. **4–6**, yields the full cascade model:

$$\frac{dc(l,t)}{dt} = -\frac{\gamma V_f(l)}{V_s}c(l,t) + \frac{\gamma}{V_s}\sum_{m=1}^\infty 2^{2m}\left[V_f(2l) - V_f(l)\right]c(2^m l,t). \quad [8]$$

Note that because shorter tubes require higher fluid elongational rates to break and very short tubes require a very high elongational rate to break, $V_f(l)$ is a monotonically increasing function

$$V_f(l) \geq V_f(l') \quad \text{for} \quad l \geq l' \quad [9]$$

and

$$\lim_{l\rightarrow 0} V_f(l) = 0. \quad [10]$$

Eqs. **8–10** define the model of tube breaking used in the analysis.

It has been experimentally observed that DNA nanotubes can join end-to-end (45). To assess the effect end-joining might have on attempts to extract $V_f(l)$ from the data, a more complete model incorporating end-joining of DNA nanotubes was considered. This

"end-to-end joining model" considers the full cascade of bifurcations and is given by

$$
\frac{dc(l,t)}{dt} = -\frac{\gamma V_f(l)}{V_s} c(l,t) + \frac{\gamma}{V_s} \sum_{m=1}^{\infty} 2^{2m} \left[V_f(2l) - V_f(l) \right] c(2^m l, t)
$$
$$
- \int_0^{\infty} k(l,l') c(l,t) c(l',t)\, dl' + \int_0^{l} k(l', l-l') c(l',t) c(l-l',t)\, dl',
$$

[11]

where $k(l,l')$ is the second-order rate constant for the joining of two tubes, one of length l, the other of length l' to a tube of length $l+l'$. The first integral on the right-hand side gives the rate of loss of tubes of length l due to joining with another tube. The second integral on the right-hand side gives the rate of production of tubes of length l due to the joining of a tube of length l' with a tube of length $l-l'$. It is straightforward to show that total tube length is conserved in this more complete model, that is,

$$
\frac{d}{dt} \int_0^{\infty} l c(l,t)\, dl = 0.
$$

[12]

The full cascade model also satisfies this condition because condition **3** was imposed in building the model.

There are few data available on the rate constant $k(l,l')$. Using the expression for the Stokes drag on a rod of length l and radius r, the relationship between mobility and diffusion, and the relation between diffusion constants and reaction rates for diffusion-controlled reactions (46, 47), we modeled this rate constant as

$$
k(l,l') = \kappa \frac{12 k_B T}{\eta} \left(\frac{\ln(l/R)}{l/R} + \frac{\ln(l'/R)}{l'/R} \right),
$$

[13]

where R is the tube diameter, $0 < \kappa < 1$ accounts for the fraction of productive collisions, k_B is the Boltzmann constant, and T is the absolute temperature [see *SI Appendix*, section 7 for details, including a comparison with the result of Hill (48)]. With $\kappa = 1$, this expression is an upper bound for diffusion-controlled end-joining.

However, it is known that DNA hybridization is not diffusion-controlled, i.e., the majority of collisions are unproductive (49). Based on hybridization rate constants measured for 10-mers (50), we estimated a reference value of $\kappa_{ref} = 2.2 \times 10^{-4}$ (*SI Appendix*, section 7). Using the methods described below to extract $V_f(l)$ from the experimental data, and assuming various values for κ, we found that there was minimal change in the quality of fit ($< 5\%$) and in the inferred fragmentation volumes ($< 20\%$ for $1/4 \ \mu m \le l \le 18 \ \mu m$ and < 10-fold for $l = 1/8 \ \mu m$) for $0 \le \kappa/\kappa_{ref} \le 1.2$, but the quality of fit was 3.3-fold worse for $\kappa/\kappa_{ref} \sim 12$. From this we concluded both that κ_{ref} is a reasonable estimate and that neglecting end-joining is satisfactory for analysis of the experiment. Consequently, most of the data analysis was carried out using the full cascade model rather than the end-to-end joining model. The analysis was facilitated by the fact that Eq. **8** can be solved analytically given V_f in look-up table form and knowledge of $c(l,0)$. The solutions are presented in *SI Appendix*, section 4.

Data Analysis for Extracting the Fragmentation Volume. The experimentally measured tube length distribution at $t = 0$ obtained by partitioning the measured tube lengths in $1/32$-μm-wide bins served as the initial value data (*SI Appendix*, Fig. S2). A stochastic search method was used to find a piecewise linear and continuous $V_f(l)$, constrained to start at zero and to be monotonic so as to satisfy Eqs. **9** and **10**, which resulted in the best fit (weighted mean-

squared error) between the measured concentration distribution $c(l,t)$ and the computed concentration distribution $c_c(l,t)$. The fitness function, as well as other details of the data analysis process, is given in *SI Appendix*, section 6. For the full cascade model, Eqs. **8**–**10**, the best-fit computed concentration distribution compared with the measured concentration distribution is shown in *SI Appendix*, Figs. S7 and S8 for the assay buffer and in *SI Appendix*, Fig. S10 for the case of ocean water. The results of extracting V_f from the buffer and ocean water data using the full cascade model are shown in Fig. 5. One sees that the fragmentation volume functions $V_f(l)$ for the buffer and ocean water overlap within the uncertainty of the fit. Using Eq. **1**, V_f can be expressed as a function of the elongational flow rate $\dot{\epsilon}$, as indicated by the x-axis labels above the figure.

In the large l region (as defined below), the plot of Fig. 5 does not depend on $n(l,l')$ and is thus model independent, making the values for V_f extracted in this region particularly robust. This follows from the fact that our initial tube length distributions fall off rapidly for large l so that the distribution effectively cuts off at a maximum tube length l_m. Consequently, new tubes with lengths in the region $l_m/2 < l \le l_m$ will not be produced, and the change in $c(l,t)$ as a function of time will only be due to loss of tubes from this part of the distribution through tube breakage. In this region, the length distribution simply decays exponentially with the decay constant $\gamma V_f(l)/V_s$, as per the first term of Eq. **8**. Hence, in this interval a fit to the exponential decay of $c(l,t)$ suffices to extract V_f, as is shown in Fig. 5 and *SI Appendix*, Fig. S11. The theory we have presented is necessary to extract V_f in the region $0 \le l < l_m/2$ because here the dynamics is complicated by the addition of new tubes from the breakage of tubes of length $l_m/2 < l \le l_m$.

As an aside, note that rod-like DNA nanostructures could be fabricated with well-defined lengths (43, 51) and designed to split exactly in the middle by introducing a "weak spot" with fewer
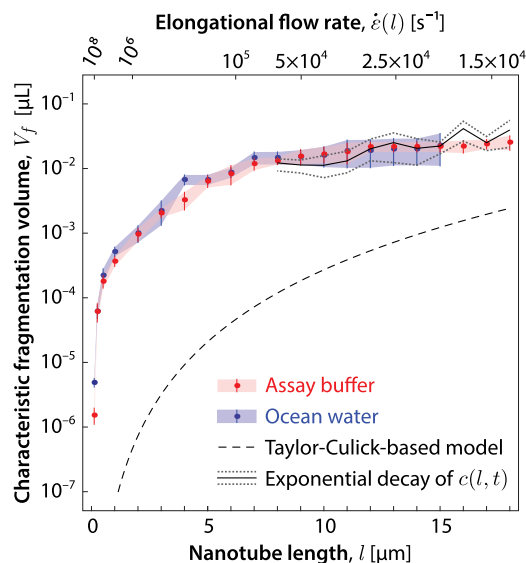

Fig. 5. Characteristic fragmentation volume V_f for tubes in the length bin interval $l \pm 1 \ \mu m$ for assay buffer (red) and ocean water (blue) data. The best-fit V_f function for assay buffer is similar to the best-fit V_f function for ocean water, which indicates that DNA nanotube fragmentation occurs in a similar fashion in the two liquids. The simple theoretical estimate of V_f using the Culick and Taylor model of film hole dynamics (black dashed line) falls below our data, as expected, due to the neglect of hydrodynamic effects within bursting bubbles that are not easily modeled. For sufficiently long nanotubes ($l > 8 \ \mu m$), the best-fit V_f for assay buffer data (blue) is similar to the V_f values (solid black line ± gray dotted lines) extracted from the exponential decay of $c(l,t)$ (*SI Appendix*, Fig. S11). Error bars represent SEM (*SI Appendix*, section 6.4).

helices in the cross-section. Such structures could be used to determine $V_f(l)$ for the length l of the structure simply by monitoring the exponential decay due to breakage, because the possibility of breakage at multiple locations can be discounted. However, compared with using tile-based DNA nanotubes that have a broad length distribution, this approach has the disadvantage that, for a given nanostructure, V_f can only be determined at one l.

Some insight into where most of the fragmentation is occurring can be obtained by considering the size of V_f. The data of Fig. 5 suggest that $V_f(l)$ approaches an asymptotic value of 2.6×10^{-2} μL for large l. The bubbles in this experiment have an air volume equivalent to a sphere of radius 1.3 mm. For bubbles of this size, surface tension rather than gravity dominates in determining the bubble shape. These bubbles in isolation rest largely below the water surface and maintain a nearly spherical shape with a small cap protruding above the water surface that is 100 nm thick as measured by Lhuissier and Villermaux (28). The depth of the bubble foam formed under the fast bubbling rate is roughly three bubble diameters thick (Fig. 2B). Pushed up by the buoyancy of the bubbles below, the bubbles near the top of the film can be expected to protrude higher and have cap films and foam facet films with areas somewhat larger than that of an isolated bubble. However, one expects the film thickness to be comparable to that of an isolated bubble due to similar surface-tension–driven film draining. A generous overestimate of 1.1×10^{-3} μL for the film volume per bubble is obtained by multiplying half the bubble surface area by 100 nm. The 20-fold discrepancy with the measured fragmentation volume implies either that the film is considerably thicker than 100 nm—perhaps due to the context of the foam—or that substantial fragmentation occurs outside the cap region, i.e., in the meniscus where the film thickness increases, in the interstices between bubbles of a foam, or in the bulk.

As indicated in the Introduction, a crude estimate for V_f associated with fluid stretching along the length of the perimeter can be obtained from the Taylor–Culick model of film hole dynamics, where the volume of fluid swept up by the hole before the elongational rate falls below a particular value $\dot{\epsilon}$ is given by $V_f = 2\pi\sigma/\rho\dot{\epsilon}^2$. Using Eq. **1**, one obtains $V_f = 1.4 \times 10^9 \mathrm{m}^{-1} \times l^4/\ln^2(l/2R)$, where we have used $\rho = 1$ g/cm^3 and $\sigma = 73$ dyn/cm for the density and surface tension of water, and l is the nanotube length. This relationship is plotted as a dashed line in Fig. 5.

As we have already mentioned, within this model, energy conservation requires that half the surface-tension energy released must be dissipated within the toroid, suggesting the existence of additional microscale fluid flows within the toroid (18, 24) that must be taken into account to accurately predict V_f. In addition, an accurate calculation would require taking into account the geometry of a bubble contacting a water surface (26), which differs from that of a planar film of uniform thickness, and mechanisms that give rise to instabilities and droplet spray along the hole perimeter (28, 52). In summary, the V_f of the Taylor–Culick-based model, plotted in Fig. 5, is a loose lower bound above which the data must lie.

By computing the Péclet number Pe, we can now confirm that misalignment of the nanotube from the direction of the elongational flow due to Brownian motion is not significant. In the present case, Pe can be taken to be the ratio of the elongational rate to the rotational diffusion constant $\mathrm{Pe} = \dot{\epsilon}/D_r$ (53), where the rotational diffusion constant is given by $D_r = 3k_BT \ln(l/R)/\pi\eta l^3$ (54) and l is the length of the tube before scission. Therefore, the Pe number for nanotubes that experience midpoint scission can be estimated based on the experimentally measured length-dependent $\dot{\epsilon}$ (Eq. **1**), from which we see that Pe increases monotonically with tube length l. For the range of nanotubes in Figs. 4 and 5 that experience substantial fragmentation ($l \geq 1/8$ μm), Pe was estimated to be $>1.4 \times 10^4$. By analyzing torques within the fluid (47, 55), we showed that Pe is the inverse of the mean-squared angular deviation of the nanotube axis from the elongational direction and therefore $\sqrt{\langle\theta^2\rangle} < 8.3 \times 10^{-3}$ rad (*SI Appendix*, Eq. **S88** and section 8). Taken together, the high Pe number and small $\langle\theta^2\rangle$ indicate that the effects of diffusional reorientation are expected to be negligible.

Discussion

Our experiments indicate that DNA nanotube fragmentation can serve as a probe of elongational flows generated at small scales in time-varying complex fluid flows, where imaging of tracer particles would be impractical. We have used DNA nanotube fragmentation to probe the elongational rates in the fluid flows generated by bursting bubbles in aqueous solutions, including ocean water. The DNA nanotube fragment distributions we have measured indicate more intense elongational flow rates than those predicted using the Culick (22) and Taylor (23) model. A more accurate model will have to take into account small-scale hydrodynamic flows occurring within the bubble film. The ability of a bursting bubble to fragment objects suspended within the bubble film has been characterized by the fragmentation volume $V_f(\dot{\epsilon})$, which is the volume of fluid subject to elongational rates in excess of $\dot{\epsilon}$. Although our data for two different bubble sizes did not reveal a strong size dependence of the fragmentation volume, further exploration using a wider range of bubbles sizes could be illuminating. In addition, it will depend on surface tension, viscosity, and the presence of surfactants. The exploration of these dependencies is left to future work. However, when these dependencies are sufficiently well known, the fragmentation volume can be used to determine the rate with which small objects will be broken, by passage through bubbles, in bodies of water ranging from oceans to bioreactors, provided the concentration of the objects, their susceptibility to elongational flows [i.e., $\dot{\epsilon}(l)$], and the size spectrum rate for the bubble production are known.

Whether biological organisms use the energy available in bursting bubbles to aid clonal reproduction and dispersal is not known. However, measurements of the tensile strength of microorganisms suggest that this is a possibility. For example, Stocks and Thomas (56) have measured a tensile strength of $T = 1.0$ μN for the filamentous bacterium *Saccharopolyspora erythraea* grown in a fermentation tank. A hypha diameter of 180 nm and a mean hypha length of 60 μm was reported for this organism. Using these numbers, Eq. **1** yields $\dot{\epsilon} = 1.8 \times 10^6$ s^{-1} for the elongational rate needed to break these hypha in two. This is two orders of magnitude below the maximum elongational rates inferred from DNA nanotube breakage (Fig. 5).

Protobionts may have used the energy available in bursting bubbles to induce cell division without the need for complicated molecular machinery. In *SI Appendix*, section 9, we present a calculation [using the tensile strength of an analogous substance (57)] that estimates that the tubular vesicle investigated by Szostak's group (10–12) can be broken into 1-μm sections under an elongational rate of $\dot{\epsilon} = 2.5 \times 10^6$ s$^{-1} \times n$, where n is the number of lamella in the vesicle. This is also well within the range of $\dot{\epsilon}$ that we have inferred for bursting bubbles. Bursting bubbles therefore provide ample hydrodynamic forces to drive this protocell division process.

Bursting bubbles are also capable of fragmenting covalently linked polymers such as duplex DNA. Using 6 nN as the suddenly applied force needed to break a covalent bond (58–60) and 1 nm as the radius for duplex DNA, one finds from Eq. **1** that an elongational rate of 1.0×10^8 s^{-1} is able to fragment duplex DNA into sections 0.33 μm long. Long-chain synthetic polymers, in which the monomer units are covalently linked together by a single bond, have a radius that is typically less than half that of duplex DNA and can thus be fragmented into segments as small as those of duplex DNA. It is conceivable that bursting bubbles may play some role in degrading plastics and biomaterials within

the ocean (61) and may aid in the dispersal of natural and man-caused oil slicks (62).

Our use of self-assembled DNA nanostructures to probe hydrodynamic flows within bursting bubbles suggests that DNA nanotechnology can provide tools to explore hydrodynamics at short length scales and fast time scales that would be difficult to investigate by other means. Among the other intense transient ocean fluid flows that are effective in shearing small objects in modern oceans and that may have aided reproduction of the protobiont are those associated with rain impacts on the ocean surface and with whitecap formation during wave breaking. DNA-based probes may serve as useful tools to characterize the fragmentation potential of these fluid flows as well, particularly because, as our experiments have shown, such probes can function in ocean water.

Materials and Methods

DNA Nanotubes. The design and characterization of the nanotubes is discussed in ref. 32. A stock solution of DNA nanotubes was prepared by mixing 7 DNA strands (Integrated DNA Technologies, Inc.; SI Appendix, Table S1 and Fig. S1) at equimolar concentration of 3.50 μM in a buffer consisting of 1 × TAE (40 mM Tris-acetate and 1 mM EDTA), pH 8.3 with 12.5 mM Mg-acetate and then slowly annealing from 90 °C to room temperature (∼25 °C) over the course of a day in a Styrofoam box. The nanotube stock solution was then diluted by a factor of 20 for the experiments, which were performed at room temperature.

Imaging. The images were acquired with a custom-built prism-based TIRF upright microscope, as described in refs. 32, 34. A solid-state green laser (GCL-025, 25 mW, CrystaLaser) equipped with an adjustable power supply (CL2005, CrystaLaser) provides the excitation beam at 532 nm. The excitation light was filtered with a 532-nm laser filter (Z532/10×, Chroma). The filtered excitation beam passed through a quarter-wave plate (Thorlabs) to produce a circularly polarized light wave, which effectively has uniform polarization to counter the fluorescence dependence on the relative orientation between fluorophore and the polarization of excitation light. Two mirrors (Thorlabs) were used to guide the illumination beam to the field of view below the imaging optics. Another mirror (Thorlabs) and a 15-cm focusing lens (CVI Laser Optics) steered the excitation beam onto a Suprasil 1 right-angle prism (CVI Laser Optics) at ∼0 ° from the horizon to produce a weakly focused illumination spot directly below the objective. We calculated that the incoming angle between the incoming laser and the normal vector of the microscope slide is sufficiently larger than critical angle for evanescent wave to occur at the interface between glass and liquid, where the sample and focal plane of the objective are located.

DNA nanotubes resided inside a glass capillary tube that was optically coupled with the prism by a thin layer of immersion oil. The emitted photons were captured by a 60× 1.2-N.A. water immersion objective (Nikon) and focused to the electron multiplier CCD camera (C9100-02, Hamamatsu) by a 20-cm lens tube (double achromat, CVI Laser Optics). The combination of the high brightness and photostability of Cy3-labeled DNA nanotubes, low background from RCA-cleaned microscope slides, and efficient light collection produce images with high signal-to-noise ratio.

Nanotube Length Measurement. Following a procedure previously reported (32, 34) for the microscopy assay, a 1-μL volume of fluid was withdrawn and immediately diluted by a factor of 40 in buffer. A 5-μL volume of this diluted sample was then deposited between an RCA-cleaned (63) microscope slide and RCA-cleaned coverslip and then imaged. We found that DNA nanotubes stuck readily to this surface.

Contour lengths of Cy3-labeled DNA nanotubes were analyzed using ImageJ (64). Nanotube detection was performed manually. The maximum pixel intensity in each detected feature was used to exclude aggregates of DNA nanotubes and colocalized DNA nanotube fragments. Moreover, all features whose maximum pixel intensities were above the saturation level of the camera were excluded from the length measurement. For each detected nanotube, the number of emitted photons Φ_{NT} was measured as a proxy for the contour length l. Briefly, two rectangular region of interests R_1 and R_2 were selected manually to satisfy these criteria: (*i*) the nanotube of interest was the only detected feature inside R_1 and (*ii*) R_1 was well inside R_2. Then, the mean local background φ_B was calculated by $\varphi_B = (\Phi_2 - \Phi_1)/(A_2 - A_1)$, where Φ_1 and Φ_2 are the sum of all pixel intensities in R_1 and R_2, respectively, and A_1 and A_2 are the areas of regions R_1 and R_2, respectively. The number of photons emitted by a nanotube was determined to be $\Phi_{NT} = \Phi_1 - \varphi_B A_1$. Finally, in each image, the contour length and photon numbers of the longest nanotube (whose length, $l > 3$ μm, could be easily measured) provided a calibration factor for the linear conversion of Φ_{NT} to l. This technique is robust to the curvature of DNA tubes and to the image sharpness. Moreover, the photon-counting method allows for the determination of nanotube lengths even for fragments that are not optically resolved.

In other experiments, our prism-based TIRF microscope proved capable of detecting single Cy3 molecules. Despite this sensitivity, here we obtained very low false-positive detection rates with our experimental procedure, as indicated by the counts of short nanotubes at early times (before 2 min of bubbling) that are plotted in Fig. 4C. On the other hand, we cannot exclude the possibility that some DNA nanotubes, e.g., those shorter than $1/32$ μm, did not stick as readily to the RCA-cleaned glass, or were not counted due to photobleaching. However, the constancy of total measured tube length (Fig. 4A) suggests that this effect was not significant. Furthermore, if our experimental methods undercounted short nanotubes, then an even larger maximal elongational rate could be inferred than what we have reported here, making our reported value a lower bound.

Ocean Water. The ocean water was collected from a rock breakwater in San Buenaventura State Beach in Ventura, California. For use in the experiments, a 1-mL sample of ocean water was filtered through a Millex-GP filter unit (Millipore, 0.22-μm pore size) using a syringe.

1. Khou M, Paul NA, Wright JT, Steinberg PD (2007) Intrinsic factors influence the attachment of fragments of the green alga *Caulerpa filiformis*. *J Exp Mar Biol Ecol* 352(2):331–342.
2. Highsmith RC (1982) Reproduction by fragmentation in corals. *Mar Ecol-Prog Ser* 7(2):207–226.
3. Coffroth MA, Lasker HR (1998) Population structure of a clonal gorgonian coral: The interplay between clonal reproduction and disturbance. *Evolution* 52(2):379–393.
4. Adamec F, Kaftan D, Nedbal L (2005) Stress-induced filament fragmentation of *Calothrix elenkinii* (cyanobacteria) is facilitated by death of high-fluorescence cells. *J Phycol* 41(4):835–839.
5. Bennett A, Bogorad L (1973) Complementary chromatic adaptation in a filamentous blue-green alga. *J Cell Biol* 58(2):419–435.
6. Oparin AI, Morgulis S (1953) *The Origin of Life* (Dover, New York), p 193.
7. Cairns-Smith AG (1966) The origin of life and the nature of the primitive gene. *J Theor Biol* 10(1):53–88.
8. Cairns-Smith AG (2008) Chemistry and the missing era of evolution. *Chemistry* 14(13):3830–3839.
9. Bullard T, Freudenthal J, Avagyan S, Kahr B (2007) Test of Cairns-Smith's 'crystals-as-genes' hypothesis. *Faraday Discuss* 136(1-2):231–245.
10. Budin I, Debnath A, Szostak JW (2012) Concentration-driven growth of model protocell membranes. *J Am Chem Soc* 134(51):20812–20819.
11. Budin I, Szostak JW (2010) Expanding roles for diverse physical phenomena during the origin of life. *Annu Rev Biophys* 39:245–263.
12. Zhu TF, Szostak JW (2009) Coupled growth and division of model protocell membranes. *J Am Chem Soc* 131(15):5705–5713.
13. Schulman R, Yurke B, Winfree E (2012) Robust self-replication of combinatorial information via crystal growth and scission. *Proc Natl Acad Sci USA* 109(17):6405–6410.
14. Collins SR, Douglass A, Vale RD, Weissman JS (2004) Mechanism of prion propagation: Amyloid growth occurs by monomer addition. *PLoS Biol* 2(10):e321.
15. Alvarado AS (2000) Regeneration in the metazoans: Why does it happen? *BioEssays* 22(6):578–590.
16. Deane GB, Stokes MD (2002) Scale dependence of bubble creation mechanisms in breaking waves. *Nature* 418(6900):839–844.
17. Cunliffe M, et al. (2013) Sea surface microlayers: A unified physicochemical and biological perspective of the air–ocean interface. *Prog Oceanogr* 109:104–116.
18. Cherry RS, Hulle CT (1992) Cell death in the thin films of bursting bubbles. *Biotechnol Prog* 8(1):11–18.
19. Dupré A (1867) Sixième mémoire sur la théorie méchanique de la chaleur. *Ann Chim Phys* 4(11):194–220.
20. Rayleigh L (1891) Some applications of photography. *Nature* 44(1133):249–254.
21. Ranz WE (1959) Some experiments on the dynamics of liquid films. *J Appl Phys* 30(12):1950–1955.
22. Culick FEC (1960) Comments on a ruptured soap film. *J Appl Phys* 3(6):1128–1129.
23. Taylor G (1959) The dynamics of thin sheets of fluid. III. Disintegration of fluid sheets. *Proc R Soc Lond A* 253(1274):313–321.

24. Pandit AB, Davidson JF (1990) Hydrodynamics of the rupture of thin liquid films. *J Fluid Mech* 212:11–24.
25. Spiel DE (1998) On the births of film drops from bubbles bursting on seawater surfaces. *J Geophys Res* 103(C11):24907–24918.
26. Boulton-Stone JM, Blake JR (1993) Gas bubbles bursting at a free surface. *J Fluid Mech* 254:437–466.
27. Dey D, Boulton-Stone JM, Emery AN, Blake JR (1997) Experimental comparisons with a numerical model of surfactant effects on the burst of a single bubble. *Chem Eng Sci* 52(16):2769–2783.
28. Lhuissier H, Villermaux E (2012) Bursting bubble aerosols. *J Fluid Mech* 696:5–44.
29. Franklin MP, et al. (2005) Bacterial diversity in the bacterioneuston (sea surface microlayer): The bacterioneuston through the looking glass. *Environ Microbiol* 7(5):723–736.
30. Gladyshev M (2002) *Biophysics of the Surface Microlayer of Aquatic Ecosystems* (IWA, London).
31. Liss PS, Duce RA (1997) *The Sea Surface and Global Change* (Cambridge Univ Press, Cambridge, UK).
32. Yin P, et al. (2008) Programming DNA tube circumferences. *Science* 321(5890): 824–826.
33. Smith DE, Chu S (1998) Response of flexible polymers to a sudden elongational flow. *Science* 281(5381):1335–1340.
34. Hariadi RF, Yurke B (2010) Elongational-flow-induced scission of DNA nanotubes in laminar flow. *Phys Rev E* 82(4):046307.
35. Wenner JR, Williams MC, Rouzina I, Bloomfield VA (2002) Salt dependence of the elasticity and overstretching transition of single DNA molecules. *Biophys J* 82(6): 3160–3169.
36. Schiffels D, Liedl T, Fygenson DK (2013) Nanoscale structure and microscale stiffness of DNA nanotubes. *ACS Nano* 7(8):6700–6710.
37. Kantsler V, Goldstein RE (2012) Fluctuations, dynamics, and the stretch-coil transition of single actin filaments in extensional flows. *Phys Rev Lett* 108(3):038103.
38. Wandersman E, Quennouz N, Fermigier M, Lindner A, Du Roure O (2010) Buckled in translation. *Soft Matter* 6:5715–5719.
39. Reyssat É, Quéré D (2006) Bursting of a fluid film in a viscous environment. *Europhys Lett* 76(2):234–242.
40. Martin P, Buguin A, Brochard-Wyart F (1994) Bursting of a liquid film on a liquid substrate. *Europhys Lett* 28(6):421–426.
41. Goodall DG, Gee ML, Stevens G, Perera J, Beaglehole D (1998) An investigation of the critical thickness of film rupture and drainage phenomena using dual wavelength ellipsometry. *Colloid Surface A* 143(1):41–51.
42. Boulton-Stone JM (1995) The effect of surfactant on bursting gas bubbles. *J Fluid Mech* 302:231–257.
43. Douglas SM, Chou JJ, Shih WM (2007) DNA-nanotube-induced alignment of membrane proteins for NMR structure determination. *Proc Natl Acad Sci USA* 104(16): 6644–6648.
44. Graugnard E, et al. (2010) Kinetics of DNA and RNA hybridization in serum and serum-SDS. *IEEE T Nanotechnol* 9(5):603–609.
45. Ekani-Nkodo A, Kumar A, Fygenson DK (2004) Joining and scission in the self-assembly of nanotubes from DNA tiles. *Phys Rev Lett* 93(26):268301.
46. Calef DF, Deutch JM (1983) Diffusion-controlled reactions. *Annu Rev Phys Chem* 34: 493–524.
47. Riseman J, Kirkwood JG (1950) The intrinsic viscosity, translational and rotatory diffusion constants of rod-like macromolecules in solution. *J Chem Phys* 18(4):512–516.
48. Hill TL (1983) Length dependence of rate constants for end-to-end association and dissociation of equilibrium linear aggregates. *Biophys J* 44(2):285–288.
49. Wetmur JG, Davidson N (1968) Kinetics of renaturation of DNA. *J Mol Biol* 31(3): 349–370.
50. Morrison LE, Stols LM (1993) Sensitive fluorescence-based thermodynamic and kinetic measurements of DNA hybridization in solution. *Biochemistry* 32(12):3095–3104.
51. Wei B, Dai M, Yin P (2012) Complex shapes self-assembled from single-stranded DNA tiles. *Nature* 485(7400):623–626.
52. Lhuissier H, Villermaux E (2009) Soap films burst like flapping flags. *Phys Rev Lett* 103(5): 054501.
53. Manhart M (2004) Visco-elastic behaviour of suspensions of rigid-rod like particles in turbulent channel flow. *Eur J Mech B-Fluid* 23(3):461–474.
54. Tsyboulski DA, Bachilo SM, Kolomeisky AB, Weisman RB (2008) Translational and rotational dynamics of individual single-walled carbon nanotubes in aqueous suspension. *ACS Nano* 2(9):1770–1776.
55. Broersma S (1960) Rotational diffusion constant of a cylindrical particle. *J Chem Phys* 32(6):1626–1631.
56. Stocks SM, Thomas CR (2001) Viability, strength, and fragmentation of *Saccharopolyspora erythraea* in submerged fermentation. *Biotechnol Bioeng* 75(6):702–709.
57. DeSain JD, Brady BB, Metzler KM, Curtiss TJ, Albright TV (2009) Tensile tests of paraffin wax for hybrid rocket fuel grains. AEROSPACE REPORT NO. ATR-2009(8268)-1 (The Aerospace Corporation, El Segundo, CA), pp 1–20.
58. Beyer MK, Clausen-Schaumann H (2005) Mechanochemistry: The mechanical activation of covalent bonds. *Chem Rev* 105(8):2921–2948.
59. Bustamante C, Smith SB, Liphardt J, Smith D (2000) Single-molecule studies of DNA mechanics. *Curr Opin Struct Biol* 10(3):279–285.
60. Vanapalli SA, Ceccio SL, Solomon MJ (2006) Universal scaling for polymer chain scission in turbulence. *Proc Natl Acad Sci USA* 103(45):16660–16665.
61. Law KL, et al. (2010) Plastic accumulation in the North Atlantic subtropical gyre. *Science* 329(5996):1185–1188.
62. Feng J, et al. (2014) Nanoemulsions obtained via bubble-bursting at a compound interface. *Nat Phys* 10(8):606–612.
63. Braslavsky I, Hebert B, Kartalov E, Quake SR (2003) Sequence information can be obtained from single DNA molecules. *Proc Natl Acad Sci USA* 100(7):3960–3964.
64. Schneider CA, Rasband WS, Eliceiri KW (2012) NIH Image to ImageJ: 25 years of image analysis. *Nat Methods* 9(7):671–675.

Supporting Information

Hariadi et al. 10.1073/pnas.1424673112
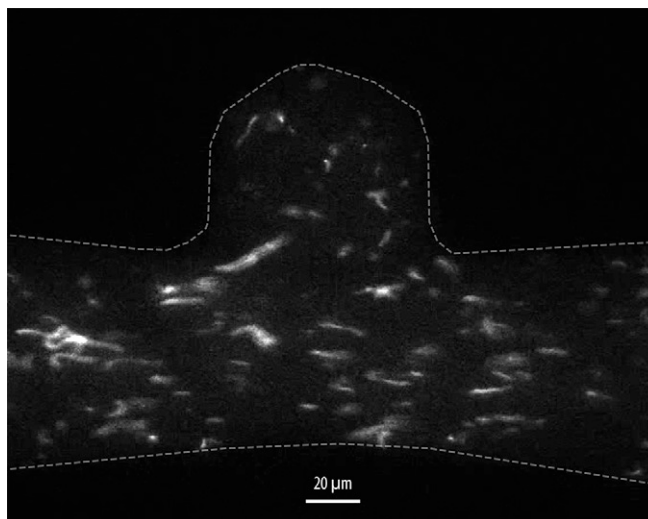
Movie S1. Fluorescence movie (1 frame per s) of Cy3-labeled DNA nanotubes in a microfluidic channel (dashed lines, height 100 μm) under slow flow rate (right to left, 47 μm/s in the center). The nanotubes experience compressional and elongational flows as they enter and exit the side chamber, respectively. The maximum elongational flow in the channel was estimated to be 1.4 /s, which is, using a conformational relaxation time of 400 ms for the nanotubes, within a factor of 2 of the critical threshold for polymer stretching (33). The measured maximum elongational flow during the bursting of a bubble (*SI Appendix*, Fig. S1) is $\sim 10^8$-fold larger than in the channel. Consequently, the elongational flow during the expansion of the bubble hole is expected to orient and stretch DNA nanotubes. Given that the longest observed nanotube in the movie is 52 μm, the maximum elongational-flow-induced tension in the channel was calculated to be 1.2 pN (Eq. **1**). The maximum generated tension in the movie is more than two orders of magnitude smaller than the critical tension to break a 7-helix DNA nanotube (455 pN). The weak hydrodynamic-induced tension is sufficient to explain the absence of nanotube scission in the movie.

[Movie S1](#)

Other Supporting Information Files

[SI Appendix (PDF)](#)

Determining hydrodynamic forces in bursting bubbles using DNA nanotube mechanics

Rizal F. Hariadi[1], Erik Winfree[2], and Bernard Yurke[3]

[1]*Applied Physics, California Institute of Technology, Pasadena, CA 91125, USA*
[2]*Bioengineering, California Institute of Technology, Pasadena, CA 91125, USA*
[3]*College of Engineering, Boise State University, Boise, ID 83725, USA*

Contents

1 Strand sequences

Name	Sequence
U1-TT-Cy3	5'- Cy3-TT-GGCGATTAGG-ACGCTAAGCCA-CCTTTAGATCC-TGTATCTGGT -3'
U2	5'- GGATCTAAAGG-ACCAGATACA-CCACTCTTCC-TGACATCTTGT -3'
U3	5'- GGAAGAGTGG-ACAAGATGTCA-CCGTGAGAACC-TGCAATGCGT -3'
U4	5'- GGTTCTCACGG-ACGCATTGCA-CCGCACGACC-TGTTCGACAGT -3'
U5	5'- GGTCGTGCGG-ACTGTCGAACA-CCAACGATGCC-TGATAGAAGT -3'
U6	5'- GGCATCGTTGG-ACTTCTATCA-ATGCACCTCC-AGCTTTGAATG -3'
T7 (modified)	5'- GGAGGTGCAT-CATTCAAAGCT-TGGCTTAGCGT-CCTAATCGCC -3'

Table S1: DNA sequences for 7-helix DNA nanotube. Apart from the oligomer T7, we have employed the published DNA sequences in ref. [1]. The modified T7 strand was designed to reduce the twist energy in the 7-helix nanotube (c.f. Ref. [2]) as shown in Fig. S1. A Cy3 fluorophore was attached to the U1 strand for fluorescent imaging
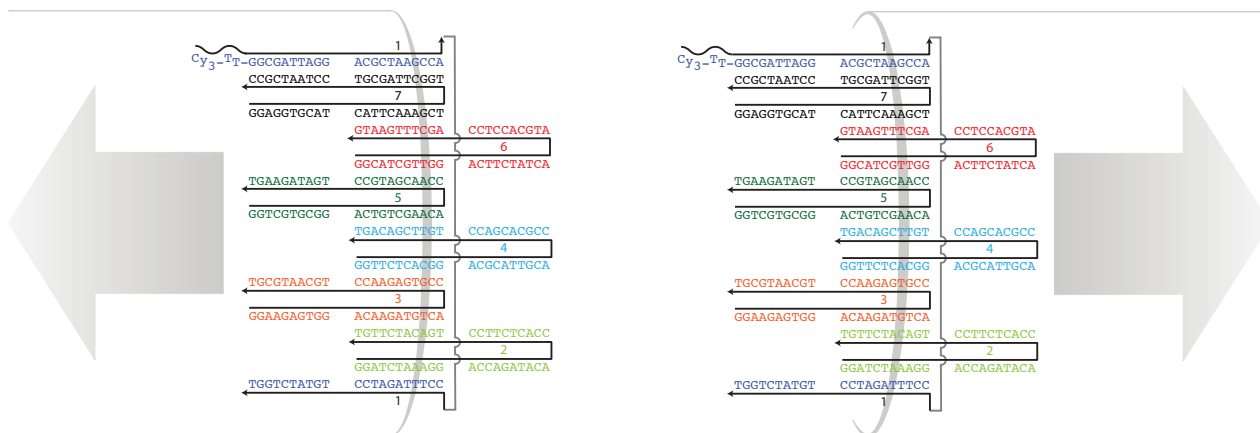

Figure S1: Strand diagram for 7-helix DNA nanotubes. Each strand has four sticky ends; each sticky end has a unique complement in its adjacent strand. The interactions between complementary sticky ends drives the nucleation and polymerization reactions to form the designed tubular structure.
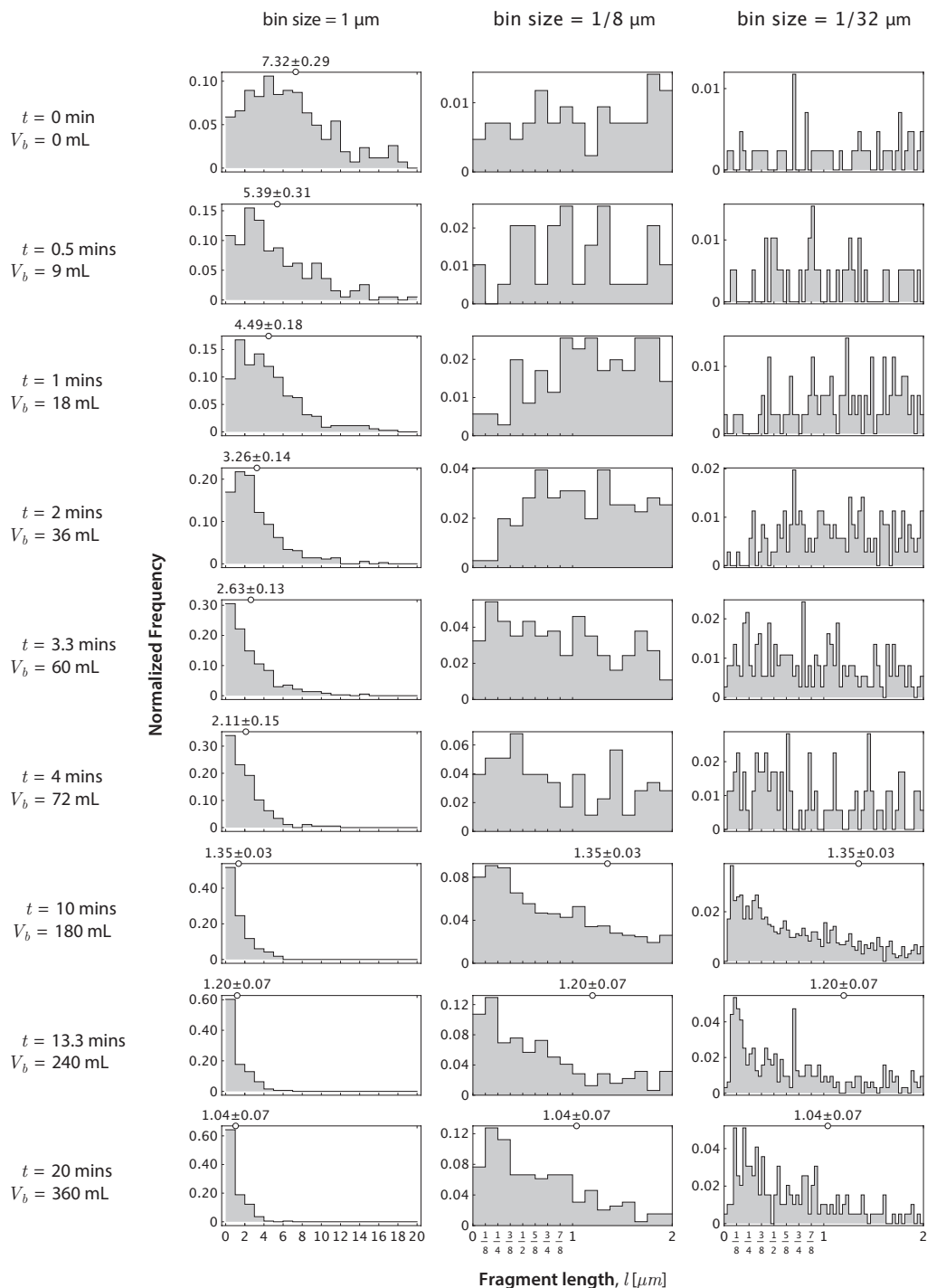
2 Supplementary Histograms

Figure S2: *Fragment length distribution for experiments in assay buffer at different exposure times with an 18 mL/min air flow rate.* The smallest bin in the histogram with bin size = 1/32 μm is relatively unaltered during the fragmentation experiments. The constant level of the 1/32 μm bin was used to infer the maximum elongational flow rate during bubble bursting.
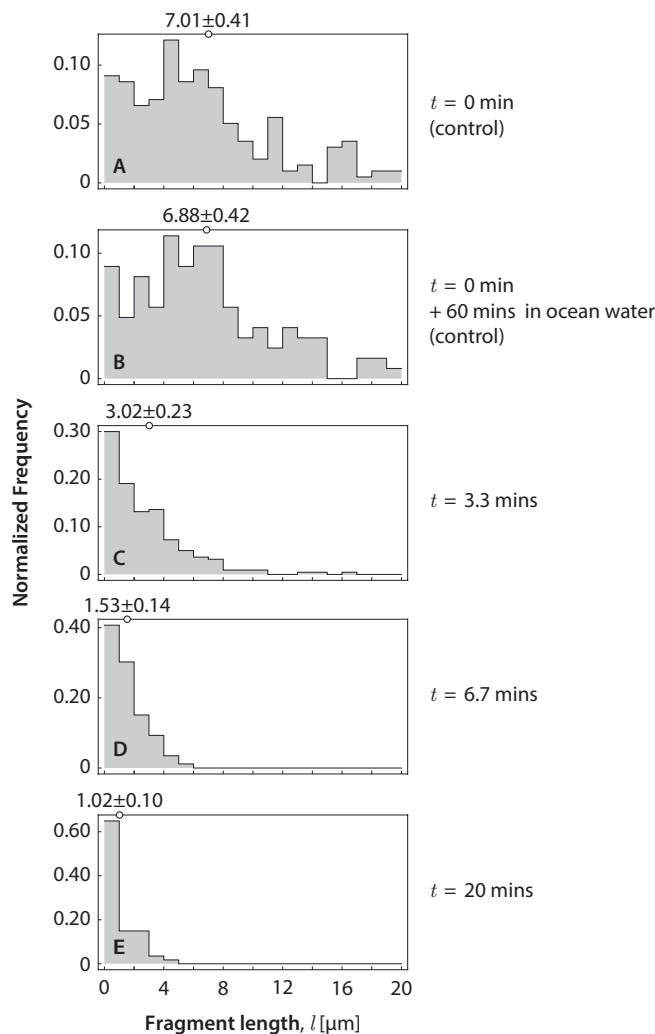
Figure S3: *Length distribution for the fragmentation experiments with ocean water.* (*A–B*) Length histograms of unperturbed DNA nanotubes in ocean water at t $= 0$ (*A*) and 1 hour (*B*). (*C–E*) Nanotube length distribution for the fragmentation experiments with ocean water at different air volume at 18 mL/min flow rate.
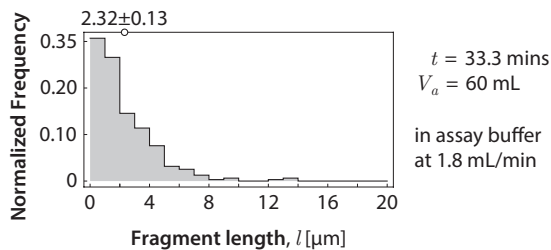

Figure S4: *The fluid flow associated with bubble inflation and formation is not responsible for fragmentation.* Fragment length distribution for the experiment with the slower flow rate (1.8 mL/min) for 33.3 min is similar to the corresponding bubble bursting experiment at 18 mL/min for 3.33 min (Fig. S2). In both cases, the total air volume was 60 mL. The $t = 0$ min length histogram in Fig. S2 provides a justifiable negative control for this experiment. Although the data in Figs. S2 and S4 were acquired on different days, the starting nanotube samples were prepared and annealed at the same time.

6.03±0.50

t = 3.3 mins
in 100 μL assay buffer
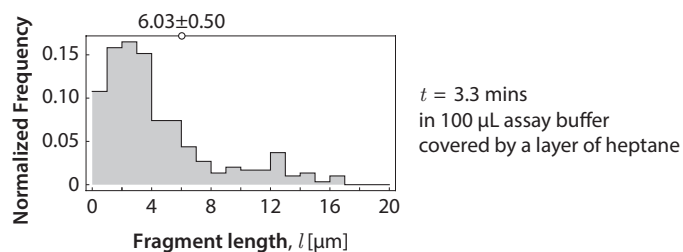covered by a layer of heptane

Figure S5: *Nanotube fragmentation is primarily due to the fluid flows associated with bubble bursting.* Fragment length histogram for the experiment in assay buffer under a layer of heptane at 18 mL/min flow rate for 3.3 mins. The length histogram is comparable to the initial nanotube length distribution (Fig. S2). The $t = 0$ min length histogram in Fig. S2 is used as control data because these experiments used the same DNA nanotube sample.
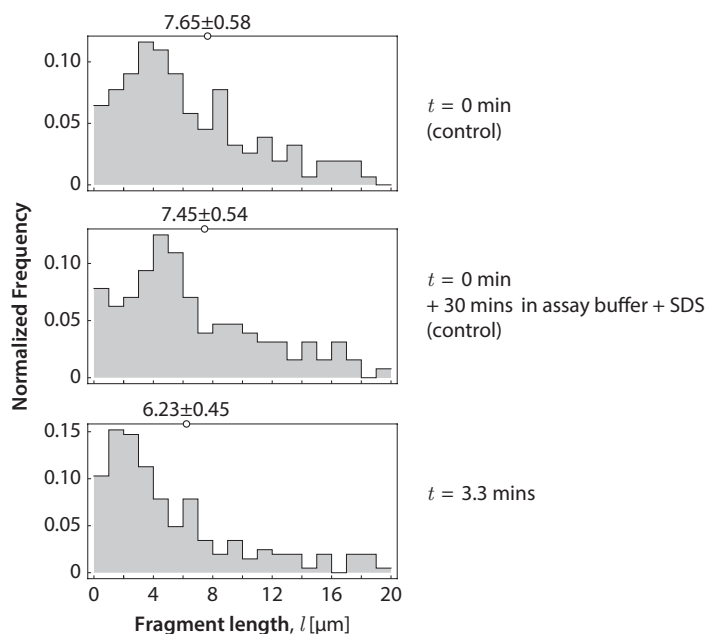

7.65±0.58

t = 0 min
(control)

7.45±0.54

t = 0 min
+ 30 mins in assay buffer + SDS
(control)

6.23±0.45

t = 3.3 mins

Figure S6: *Surface tension controls the maximum elongational rate in bubble bursting.* (*Upper–middle*) Similar length histograms before (*upper*) and after (*middle*) 30 mins incubation in 1% SDS showing the stability of DNA nanotubes in the SDS containing buffer. (*Lower*) Fragment length distribution for the control experiment in 1% SDS containing buffer. The change of length distribution is substantially less than the corresponding experiment in assay buffer (Fig. S2).
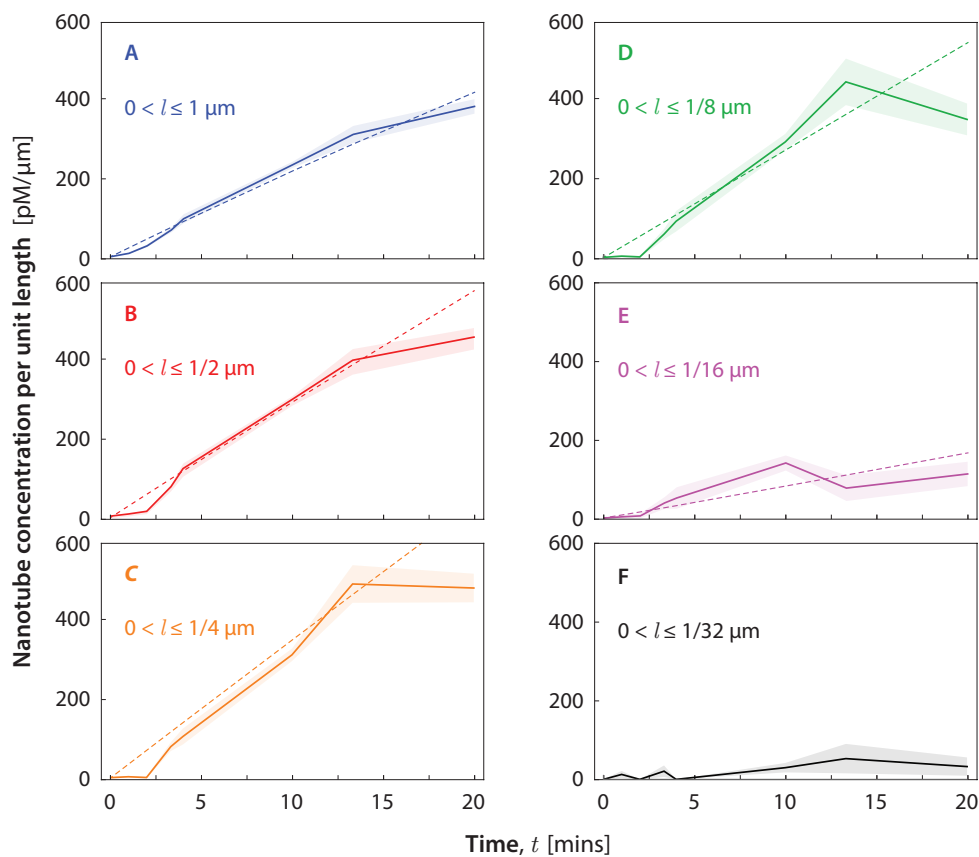
Figure S7: Experimental (solid line) and simulated (dashed, full cascade model) plots of histogram bin values for fragment lengths less than the indicated bin size over the course of the fragmentation experiment. The relative concentrations of nanotubes with $l > 1/16$ μm grow similarly with time (A–D). Those with $l < 1/16$ μm also grow, but less markedly (E). The number of nanotubes with $l < 1/32$ μm is essentially negligible over the course of the experiment (F). Shaded area indicates S.E.M. from bootstrapping.

Figure S8: Simulated (blue) and experimental (red) fragment length distributions for the fragmentation experiment with assay buffer. The simulated length histogram is generated deterministically by the full cascade model (Eq. 8 of the main text and SI sections 3 and 4), where a nanotube of length l is broken into 2^n fragments based on its $V_f(l)$. This model fits our data better than the single bifurcation model in Fig. S9.
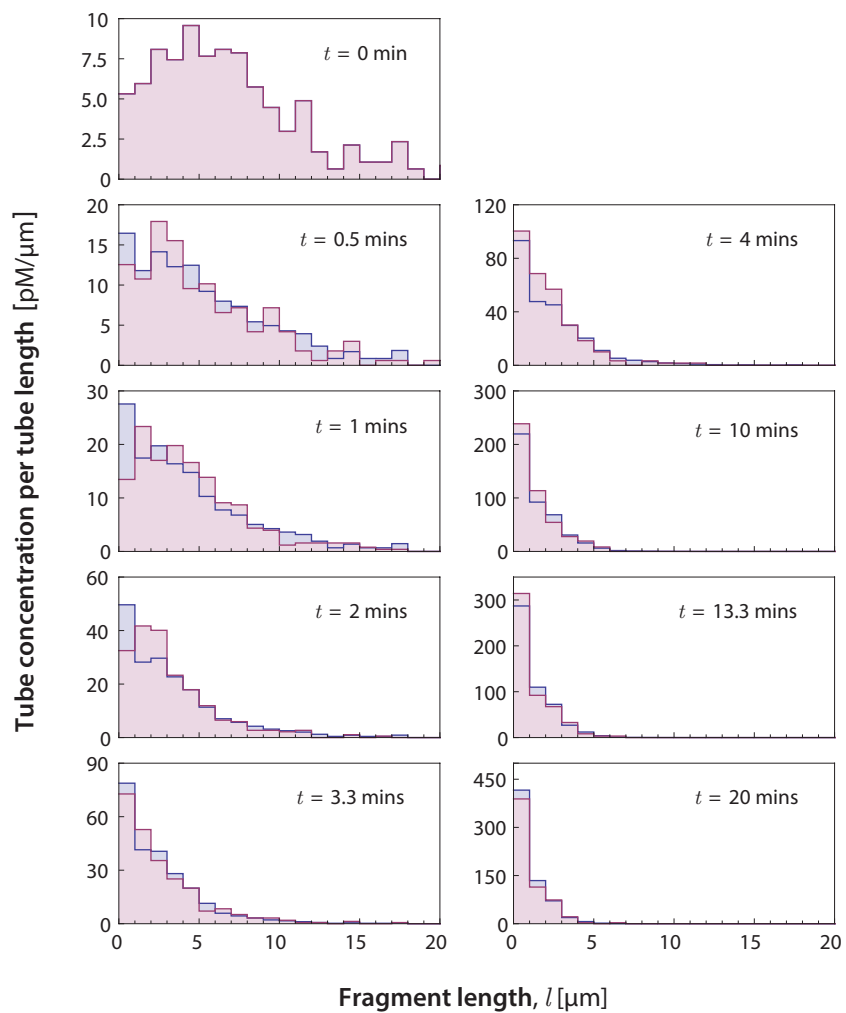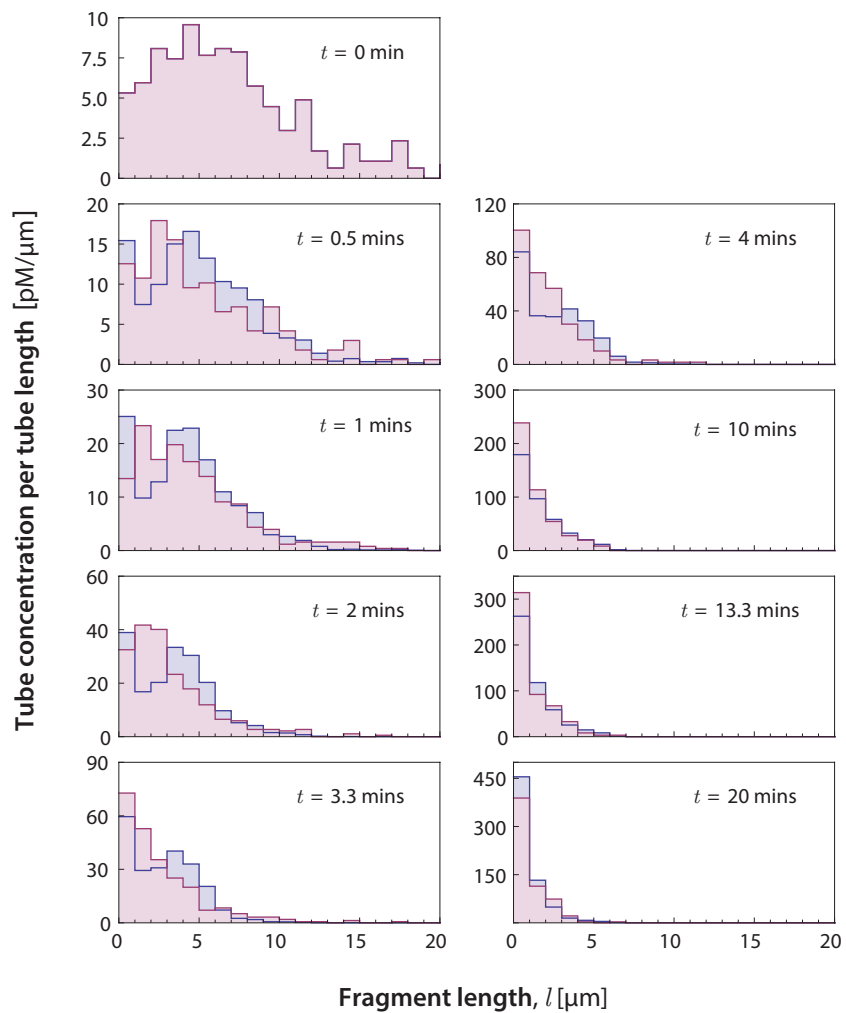
Figure S9: Simulated (blue) and experimental (red) fragment length distributions for the fragmentation experiment with assay buffer. The simulated fragment histograms are based on the single bifurcation model where nanotubes of length $2l_i$ are broken into exactly two fragments of length l_i (as described in Eq. 7 of the main text and section 5 of the SI). The value of the goodness of fit parameter, defined in Eq. (S64), is a factor of 4.1 worse than that for the full cascade model used in Fig. S8. The lower goodness of fit value is also reflected in the $c(l,t)$ distributions which exhibit a bulge, for short and intermediate times, that is absent in the experimental data.
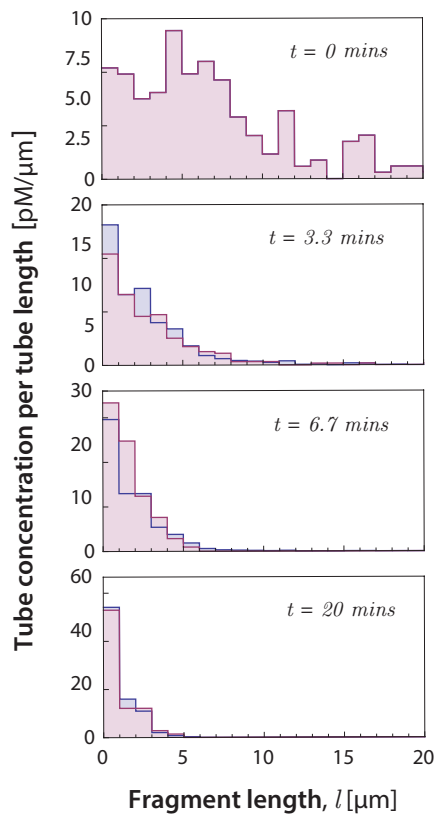
Figure S10: Simulated (blue) and experimental (red) nanotube length histogram for bubble bursting experiment in ocean water at $t=$ 0, 3.3, 6.7, and 20 mins, using the full cascade model.
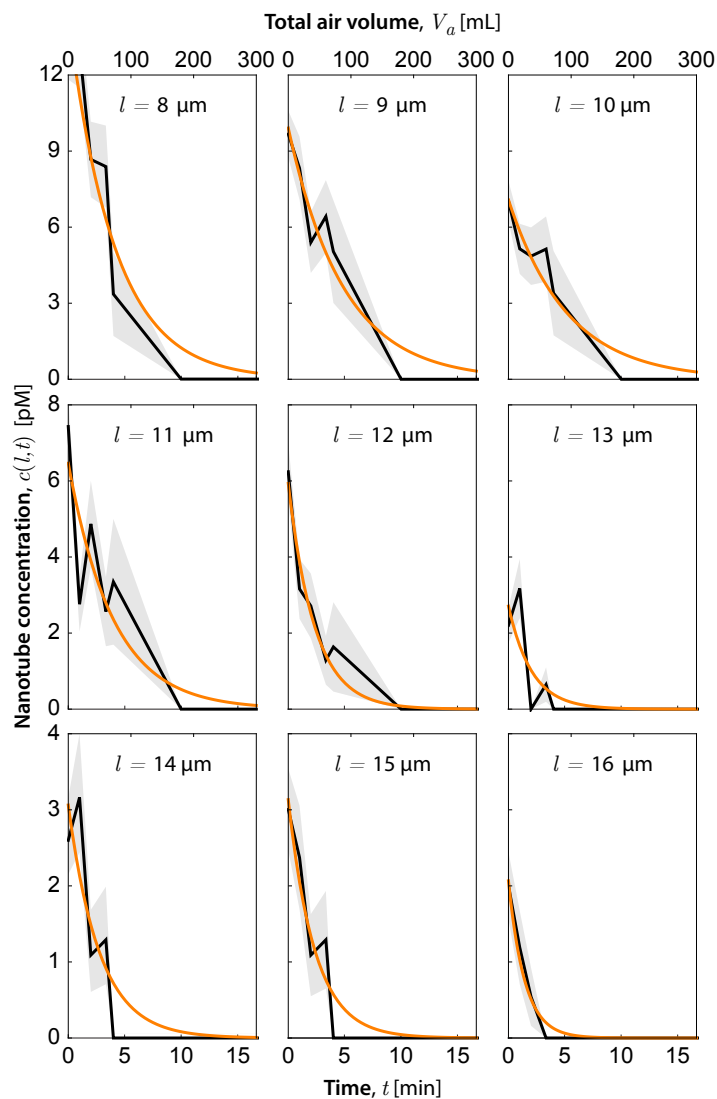
Figure S11: *Quantifying characteristic fragmentation volume $V_f(l)$ based on the evolution of nanotube concentrations.* The concentration for nanotubes in the indicated length interval $(l-1\ \mu m)$ to $(l+1\ \mu m)$ (black lines) at different time points ($t = V_a/\dot{V}_a$ with $\dot{V}_a = \gamma V_b$=18 mL/min, where γ is the bubble production rate and V_b is the measured bubble volume). Orange lines are single exponential fits of $c(l,t)$ to $\alpha e^{-\beta t}$ with characteristic decay constant $\beta = \gamma V_f(l)/V_s$, where V_s is the sample volume (100 μL). Error bars (gray-shaded regions) represent S.E.M. from bootstrapping.

3   Details for derivation of the full cascade model

Using Eqs. (4), (5), and (6) of the main text, and performing the l' integration, Eq. (2) yields

$$\frac{dc(l,t)}{dt} = -\frac{\gamma V_f(l)}{V_s}c(l,t) + \frac{\gamma}{V_s}\sum_{m=1}^{\infty} 2^{2m}p_m(2^m l)V_f(2^m l)c(2^m l, t). \tag{S1}$$

As a consistency check, again using Eqs. (4), (5), and (6), and performing the l' integration, Eq. (3) yields the condition

$$\sum_{m=1}^{\infty} p_m(l) = 1 \tag{S2}$$

which we know must hold, since $p_m(l)$ is the conditional probability that a tube of length l will fragment into 2^m tubes when it breaks.

   A further simplification of the model is achieved as follows. From the definitions of the quantities on the right hand side,

$$\gamma_m(l) = \frac{\gamma}{V_s}p_m(l)V_f(l) \tag{S3}$$

is the rate that a tube of length l in the sample volume is broken into 2^m fragments and

$$\gamma_T(l) = \frac{\gamma V_f(l)}{V_s} \tag{S4}$$

is the rate that a tube of length l in the sample volume is broken. Hence, one must have

$$\gamma_T(l) = \sum_{k=1}^{\infty} \gamma_k(l). \tag{S5}$$

Since we are considering a cascade process where a tube of length l is first broken into two pieces of length $l/2$, which each in turn break into pieces of length $l/4$, we conclude that

$$\gamma_T(l/2) = \sum_{k=2}^{\infty} \gamma_k(l). \tag{S6}$$

More generally, we conclude that

$$\gamma_T(l/2^m) = \sum_{k=m+1}^{\infty} \gamma_k(l). \tag{S7}$$

From this one obtains

$$\gamma_m(l) = \gamma_T(l/2^{m-1}) - \gamma_T(l/2^m) \tag{S8}$$

for all $m \geq 1$. Using Eqs. (S3) and (S4) this yields

$$p_m(l) = \frac{V_f(l/2^{m-1}) - V_f(l/2^m)}{V_f(l)}. \tag{S9}$$

Note that the Eqs. (9) and (10) of the main text ensure that the probabilities given by Eq. (S9) are well-behaved, convergent, and satisfy Eq. (S2). Substituting Eq. (S9) into Eq. (S1) yields Eq. (8) of the main text.

4   Solutions to the differential equation for the full cascade model

For convenience, using Eqs. (S4), (S8), and (S9), Eq. (S1) can be written as

$$\frac{dc(l,t)}{dt} = -\gamma_T(l)c(l,t) + \sum_{m=1}^{\infty} 2^{2m}\gamma_m(2^m l)c(2^m l, t). \tag{S10}$$

Since this equation is linear in the $c(l, t)$ and since it describes a cascading process in which tubes are broken into 2^m fragments of equal length, the solution must have the form

$$c(l, t) = \sum_{n=0}^{\infty} f_n(l, t) c(2^n l, 0) \tag{S11}$$

where $c(l, 0)$ is the value of $c(l, t)$ at $t = 0$. Since this equation must hold for all choices of $c(l, 0)$, setting $t = 0$ yields

$$f_n(l, 0) = \begin{cases} 1 & \text{if } n = 0 \\ 0 & \text{if } n > 0 \end{cases}. \tag{S12}$$

Substituting Eq. (S11) into Eq. (S10), and rearranging the sum by diagonals, yields

$$\sum_{k=0}^{\infty} \frac{df_k(l, t)}{dt} c(2^k l, 0)$$

$$= -\gamma_T(l) \sum_{k=0}^{\infty} f_k(l, t) c(2^k l, 0)$$

$$+ \sum_{k=1}^{\infty} \sum_{m=1}^{k} 2^{2m} \gamma_m(2^m l) f_{k-m}(2^m l, t) c(2^k l, 0). \tag{S13}$$

By setting $c(2^k l, 0) = 0$ for $k > 0$, this equation yields

$$\frac{df_0(l, t)}{dt} = -\gamma_T(l) f_0(l, t). \tag{S14}$$

By setting $c(2^k l, 0) = 0$ for all k except $k = n$ where $n \geq 1$ yields

$$\frac{df_n(l, t)}{dt} = -\gamma_T(l) f_n(l, t) + \sum_{m=1}^{n} 2^{2m} \gamma_m(2^m l) f_{n-m}(2^m l, t). \tag{S15}$$

Equation (S14), with the initial condition given in Eq. (S12), is easily integrated to yield

$$f_0(l, t) = e^{-\gamma_T(l) t}. \tag{S16}$$

Equation (S15) with the initial condition given in Eq. (S12) can be formally integrated to yield, for $n > 0$,

$$f_n(l, t) = \int_0^t e^{-\gamma_T(l)(t-t')} \sum_{m=1}^{n} 2^{2m} \gamma_m(2^m l) f_{n-m}(2^m l, t') dt'. \tag{S17}$$

Since $n - m$ is always less than n, this equation can be used to obtain $f_n(l, t)$ for successively higher n. For example, for $n = 1$ this equation becomes

$$f_1(l, t) = \int_0^t e^{-\gamma_T(l)(t-t')} 2^2 \gamma_1(2l) f_0(2l, t') dt'. \tag{S18}$$

Substituting Eq. (S16) into this equation and performing the integration yields

$$f_1(l, t) = 2^2 \gamma_1(l) \frac{e^{-\gamma_T(2l) t} - e^{-\gamma_T(l) t}}{\gamma_T(l) - \gamma_T(2l)}. \tag{S19}$$

Due to the sum appearing in Eq. (S17), the number of terms in $f_n(l, t)$ grows exponentially with n. Generally $c(l, 0)$ will fall off rapidly with l for sufficiently large l. Hence, the sum in Eq. (S11) can be cut off for sufficiently large n. Still, this n can be large. For the data analysis reported here, the smallest bin size used was $\Delta l = 1/2^5 \ \mu$m and the tube lengths spanned 0 to $2^5 \ \mu$m. The largest n used in this analysis was 10. The number of terms in the

analytic expression for $f_{10}(l,t)$ is 2^9; since the number of terms grows exponentially as a function of n, computer assisted mathematics can be used to generate terms. We determined the terms diagrammatically by the method described below.

The diagrammatic method is based on the observation that each term, in the analytic expression for $f_n(l,t)$, corresponds to a particular cascade by which tubes of length l at time t are produced by the fragmentation of tubes initially of length $2^n l$ through successive encounters with bubbles. As a first step toward generating the terms of $f_n(l,t)$, it is useful to construct a list of all possible cascades by which a tube of length l can be generated from a tube of length $2^n l$. For the given n, there are are up to $n-1$ cascade steps, this maximum number corresponding to the case where the tube of length l results from a cascade in which two fragments were produced with each encounter of a bubble by the $n-1$ successive ancestors of the tube. To generate the complete list of possible cascades for the given n it is useful to generate the list of $n+1$ digit binary numbers whose binary sequence begins with 1 and ends with 1. An example of such a list is given here for the case $n=4$.

$$
\begin{array}{ccccc}
4 & 3 & 2 & 1 & 0 \\
t_4 & t_3 & t_2 & t_1 & t \\
2^4 l & 2^3 l & 2^2 l & 2l & l \\
1 & 0 & 0 & 0 & 1 \qquad\qquad 4 \to 0 \\
1 & 0 & 0 & 1 & 1 \qquad\qquad 4 \to 1 \to 0 \\
1 & 0 & 1 & 0 & 1 \qquad\qquad 4 \to 2 \to 0 \\
1 & 0 & 1 & 1 & 1 \qquad\qquad 4 \to 2 \to 1 \to 0 \\
1 & 1 & 0 & 0 & 1 \qquad\qquad 4 \to 3 \to 0 \\
1 & 1 & 0 & 1 & 1 \qquad\qquad 4 \to 3 \to 1 \to 0 \\
1 & 1 & 1 & 0 & 1 \qquad\qquad 4 \to 3 \to 2 \to 0 \\
1 & 1 & 1 & 1 & 1 \qquad\qquad 4 \to 3 \to 2 \to 1 \to 0
\end{array}
\tag{S20}
$$

Above this list of numbers, we associate a number, time, and length with each column of digits to facilitate the construction of the terms of $f_n(l,t)$ Shown to the right of the list of binary numbers is the cascade associated with each number. The zeros in the binary numbers are interpreted as steps that are skipped in the corresponding cascade. For example, the first entry in the list, 10001, corresponds to a cascade where a tube of length l was produced directly from a tube of length $2^4 l$ that was fragmented into 2^4 tubes through one encounter with a bursting bubble. The second entry in the list, 10011, corresponds to the case where a tube of length $2^4 l$ was first fragmented into 2^3 tubes of length $2l$ by an encounter with a bursting bubble. Some of these tubes in turn were broken in two to produce tubes of length l through an encounter with another bursting bubble. As a final example, the entry 11111 corresponds to the cascade in which tubes of length $2^4 l$ were broken in two to produce tubes of length $2^3 l$ through an encounter with a bursting bubble. In turn, some of these tubes were broken in two to produce tubes of length $2^2 l$ through the encounter with another bursting bubble. In turn, some of these tubes were broken in two to produce tubes of length $2l$ through an encounter with another bursting bubble. In turn, some of these tubes were broken in two to produce tubes of length l through the encounter with another bursting bubble. These tables can be used to write down the series of nested integrals that constitute a given term of $f_n(l,t)$.

The term corresponding to an entry of a table of cascades, such as that of Eq. (S20), for $f_n(l,t)$ is constructed as follows. The leftmost bit (a 1) has associated with it the time t_n and the length $2^n l$. We also associate with it the function

$$
e^{-\gamma_T(2^n l)t_n}.
\tag{S21}
$$

Suppose the next bit to the right that is nonzero has associated with it the integer r, time t_r, and the length $2^r l$. With the n to r transition we associate the integral operator

$$
2^{2(n-r)}\gamma_{n-r}(2^n l)\int_0^{t_r} dt_n e^{-\gamma_T(2^r l)(t_r-t_n)}
\tag{S22}
$$

that operates on the function Eq. (S21). Thus, with the 1 bit at r we associate the function that results when this operator operates on the function Eq. (S21):

$$
2^{2(n-r)}\gamma_{n-r}(2^n l)\int_0^{t_r} dt_n e^{-\gamma_T(2^r l)(t_r-t_n)}e^{-\gamma_T(2^n l)t_n}.
\tag{S23}
$$

Suppose the next 1 bit to the right is at the position associated with the integer s, the time t_s, the tube length $2^s l$. With the r to s transition we associate the operator

$$2^{2(r-s)} \gamma_{r-s}(2^r l) \int_0^{t_s} dt_r e^{-\gamma_T(2^s l)(t_s - t_r)} \tag{S24}$$

which has the same form as Eq. (S22). This operator operates on the function Eq. (S23) associated with the 1 bit at position r. Thus, we associate with the 1 bit at position s the function

$$2^{2(r-s)} 2^{2(n-r)} \gamma_{r-s}(2^r l) \gamma_{n-r}(2^n l)$$
$$\times \int_0^{t_s} dt_r e^{-\gamma_T(2^s l)(t_s - t_r)}$$
$$\times \int_0^{t_r} dt_n e^{-\gamma_T(2^r l)(t_r - t_n)} e^{-\gamma_T(2^n l)t_n}. \tag{S25}$$

This process is iterated. With the right most 1 bit we have associated the integer 0, the time $t = t_0$ and the length l. Let the first 1 bit to the left of this bit have associated with it the integer u, the time t_u, and the tube length $2^u l$. Applying the operator for the u to 0 transition, which also has the form Eq. (S24), to the function associated with the 1 bit at position u one obtains

$$2^{2u} \cdots 2^{2(r-s)} 2^{2(n-r)} \gamma_u(2^u l) \cdots \gamma_{r-s}(2^r l) \gamma_{n-r}(2^n l)$$
$$\times \int_0^t dt_u e^{-\gamma_T(2^s l)(t - t_u)} \cdots$$
$$\times \int_0^{t_s} dt_r e^{-\gamma_T(2^s l)(t_s - t_r)}$$
$$\times \int_0^{t_r} dt_n e^{-\gamma_T(2^r l)(t_r - t_n)} e^{-\gamma_T(2^n l)t_n}. \tag{S26}$$

This is the full term of $f_n(l, t)$ associated with the cascade

$$2^n l \to 2^r l \to 2^s l \to \cdots 2^u l \to l. \tag{S27}$$

Inverting the order of the powers of 2 appearing at the left of Eq. (S26) one sees that

$$2^{2(n-r)} 2^{2(r-s)} \cdots 2^{2(v-u)} 2^{2u} = 2^{2n}. \tag{S28}$$

Hence Eq. (S26) simplifies to

$$2^{2n} \gamma_u(2^u l) \cdots \gamma_{r-s}(2^r l) \gamma_{n-r}(2^n l)$$
$$\times \int_0^t dt_u e^{-\gamma_T(2^s l)(t - t_u)} \cdots$$
$$\times \int_0^{t_s} dt_r e^{-\gamma_T(2^s l)(t_s - t_r)}$$
$$\int_0^{t_r} dt_n e^{-\gamma_T(2^r l)(t_r - t_n)} e^{-\gamma_T(2^n l)t_n}. \tag{S29}$$

The integrations can be carried out. The general form is given by

$$\int_0^{t_0} dt_1 e^{-\gamma_0(t_0 - t_1)} \int_0^{t_1} dt_2 e^{-\gamma_1(t_1 - t_2)} \cdots$$
$$\times \int_0^{t_{n-1}} dt_n e^{-\gamma_{n-1}(t_{n-1} - t_n)} e^{-\gamma_n t_n}$$
$$= (-1)^n \sum_{m=0}^n \frac{e^{-\gamma_m t_0}}{\prod_{i=0; i \neq m}^n (\gamma_m - \gamma_i)} \tag{S30}$$

For example, one has

$$\int_0^{t_0} dt_1 e^{-\gamma_0(t_0-t_1)} e^{-\gamma_1 t_1}$$

$$= -\frac{e^{-\gamma_1 t_0}}{\gamma_1 - \gamma_0} - \frac{e^{-\gamma_0 t_0}}{\gamma_0 - \gamma_1}, \tag{S31}$$

$$\int_0^{t_0} dt_1 e^{-\gamma_0(t_0-t_1)} \int_0^{t_1} dt_2 e^{-\gamma_1(t_1-t_2)} e^{-\gamma_2 t_2}$$

$$= \frac{e^{-\gamma_2 t_0}}{(\gamma_2 - \gamma_0)(\gamma_2 - \gamma_1)}$$

$$+ \frac{e^{-\gamma_1 t_0}}{(\gamma_1 - \gamma_0)(\gamma_1 - \gamma_2)}$$

$$+ \frac{e^{-\gamma_0 t_0}}{(\gamma_0 - \gamma_1)(\gamma_0 - \gamma_2)}, \tag{S32}$$

and

$$\int_0^{t_0} dt_1 e^{-\gamma_0(t_0-t_1)} \int_0^{t_1} dt_2 e^{-\gamma_1(t_1-t_2)}$$

$$\times \int_0^{t_2} dt_3 e^{-\gamma_2(t_2-t_3)} e^{-\gamma_3 t_3}$$

$$= -\frac{e^{-\gamma_3 t_0}}{(\gamma_3 - \gamma_0)(\gamma_3 - \gamma_1)(\gamma_3 - \gamma_2)}$$

$$- \frac{e^{-\gamma_2 t_0}}{(\gamma_0 - \gamma_2)(\gamma_1 - \gamma_2)(\gamma_2 - \gamma_3)}$$

$$- \frac{e^{-\gamma_1 t_0}}{(\gamma_1 - \gamma_0)(\gamma_1 - \gamma_2)(\gamma_1 - \gamma_3)}$$

$$- \frac{e^{-\gamma_0 t_0}}{(\gamma_0 - \gamma_1)(\gamma_0 - \gamma_2)(\gamma_0 - \gamma_3)}. \tag{S33}$$

As an illustrative example, we use the diagrammatic technique to construct $f_2(l,t)$. In this case $n = 2$ and the list of all possible cascades is

$$\begin{array}{cccll}
2 & 1 & 0 & & \\
t_2 & t_1 & t_0 & & \\
2^2 l & 2l & l & & \\
1 & 0 & 1 & 2 \to 0 & T_{21} \\
1 & 1 & 1 & 2 \to 1 \to 0 & T_{22}
\end{array} \tag{S34}$$

where T_{21} and T_{22} are the names we have given to the terms of $f_2(l,t)$ for the two possible cascades. The diagrammatic techniques yield

$$T_{21} = 2^4 \gamma_2(2^2 l) \int_0^{t_0} dt_2 e^{-\gamma_T(l)(t_0-t_2)} e^{-\gamma_T(2^2 l)t_2} \tag{S35}$$

and

$$T_{22}(t_0)$$

$$= 2^4 \gamma_1(2l)\gamma_1(2^2 l)$$

$$\times \int_0^{t_0} dt_1 e^{-\gamma_T(l)(t_0-t_1)}$$

$$\times \int_0^{t_1} dt_2 e^{-\gamma_T(2l)(t_1-t_2)} e^{-\gamma_T(2^2 l)t_2}. \tag{S36}$$

Carrying out the integrations yield

$$T_{21}(t_0) = -16\gamma_2(4l)\left(\frac{e^{-\gamma_T(4l)t_0}}{\gamma_T(4l) - \gamma_T(l)} + \frac{e^{-\gamma_T(l)t_0}}{\gamma_T(l) - \gamma_T(4l)}\right). \tag{S37}$$

and

$$
\begin{aligned}
T_{22}(t_0) \\
= 16\gamma_1(2l)\gamma_1(4l) \\
\times \Bigg(\frac{e^{-\gamma_T(4l)t_0}}{[\gamma_T(4l) - \gamma_T(l)][\gamma_T(4l) - \gamma_T(2l)]} \\
+ \frac{e^{-\gamma_T(2l)t_0}}{[\gamma_T(2l) - \gamma_T(l)][\gamma_T(2l) - \gamma_T(4l)]} \\
+ \frac{e^{-\gamma_T(l)t_0}}{[\gamma_T(l) - \gamma_T(2l)][\gamma_T(l) - \gamma_T(4l)]} \Bigg).
\end{aligned}
\tag{S38}
$$

Setting $t_0 = t$, one has

$$f_2(l,t) = T_{21}(t) + T_{22}(t). \tag{S39}$$

5 Single bifurcation model

The single bifurcation model, which uses Eq. (7) instead of Eq. (6) in combination with Eqs. (2)-(5) of the main text, is also exactly solvable using the methods outline above. The solution is somewhat simpler because only fragmentation cascades in which the tubes are broken in two at each cascade step are allowed. Using main text Eqs. (4), (5), (7) and SI Eq. (S4), main text Eq. (2) yields

$$\frac{dc(l,t)}{dt} = -\gamma_T(l)c(l,t) + 4\gamma_T(2l)c(2l,t). \tag{S40}$$

Substituting Eq. (S11) into this equation yields

$$\frac{df_0(l,t)}{dt} = -\gamma_T(l)f_0(l,t) \tag{S41}$$

and, for $n > 0$,

$$\frac{df_n(l,t)}{dt} = -\gamma_T(l)f_n(l,t) + 4\gamma_T(2l)f_{n-1}(l,t), \tag{S42}$$

where the boundary conditions Eq. (S12) still apply. Using the boundary conditions these two equations can be integrated to yield

$$f_0(l,t) = e^{-\gamma_T(l)t} \tag{S43}$$

and

$$f_n(l,t) = 4\gamma_T(2l)\int_0^t e^{-\gamma_T(l)(t-t')}f_{n-1}(2l,t')dt'. \tag{S44}$$

It is now evident that the $f_n(l,t)$ can be generated from the $f_{n-1}(l,t)$ through repeated substitution, beginning with the substitution of Eq. (S43) into Eq. (S44) for $n = 1$. $f_n(l,t)$ has the same form as the term corresponding to the $111\cdots 1$ cascades of the model discussed in SI section 4 above, except the factor $\gamma_1(2l)\gamma_1(2^2l)\cdots\gamma_1(2^n)$ appearing in this term is replaced by factor $\gamma_T(2l)\gamma_T(2^2l)\cdots\gamma_T(2^n)$, see for example Eq. (S38).

6 Numerical procedures

6.1 Constructing the experimental concentration distributions

The fluorescent microscope technique, used to construct the concentration distribution $c(l,t)$ of tube lengths at various time points, produces a list of tube lengths at these time points. To produce an experimentally determined $c(l,t)$, the number of tubes n_i whose lengths l fell within each of the bin intervals $l_i < l <= l_i + \Delta l$, were counted, where Δl is the bin width which was taken to be $\Delta l = 1/32$ μm. The resulting unnormalized

concentration distribution consisted of the list of n_i as a function of the successive bin locations l_i, where $l_{i+1} = l_i + \Delta l$ and $l_0 = 0$. Since Eq. (11) of the main text is nonlinear in $c(l,t)$, the numerical concentration must be normalized. To determine the normalization constant the tube length per unit volume was calculated from the known concentration of the oligomers forming the tubes under the assumption that all the oligomers resided within the tubes. Total tube length is defined as

$$l_T = \int_0^\infty l c(l,t) dl. \tag{S45}$$

The normalization constant a that converts the n_i into the normalized concentration distribution $c_i = a n_i$ was determined by requiring

$$\sum_i (l_i + \Delta l/2) c_i \Delta l = l_T. \tag{S46}$$

The tube length per unit volume l_T was computed via

$$l_T = \frac{N_0 b_s n_f c_s}{d_f}. \tag{S47}$$

where N_0 is the Avogadro constant, $b_s = 0.34$ nm is the spacing between successive base pairs in duplex DNA, $n_f = 10.5$ also happens to be the number of base pairs for one full turn of duplex DNA (measured in base-pair stacking units, b_s) of the DNA nanotube when a complete ring of tiles is added to a tube end, $c_s = 3.5$ μM is the concentration of a given tile in the stock solution, and $d_f = 20$ is the factor by which the concentration of the stock solution is diluted in preparing the sample solution. For our system $l_T = 3.76 \times 10^{14}$ μm/L.

6.2 Averaging over a bin width

The numerically obtained c_i should be regarded as $c(l,t)$ averaged over the interrerval $l_i < l <= l_i + \Delta l$; that is,

$$c_i(t) = \frac{1}{\Delta l} \int_{l_i}^{l_i+\Delta l} c(l,t) dl. \tag{S48}$$

This matters particularly when the experimentally determined $c_i(0)$ is used as the initial concentration distribution in Eq. (S11) to calculate the model $c_i(t)$. When using binned data, one must average Eq. (S11) over a bin width such that

$$\langle c(l,t) \rangle_{l_i} = \sum_{n=0}^\infty \langle f_n(l,t) c(2^n l, 0) \rangle_{l_i} \tag{S49}$$

where the $\langle F(i) \rangle$ of a function F is defined as

$$\langle F(l) \rangle_{l_i} = \frac{1}{\Delta l} \int_{l_i}^{l_i+\Delta l} F(l) dl. \tag{S50}$$

We note that even though Δl may be small, $c(2^n l, 0)$ can be strongly varying over this interval when n is large. Similarly, $f_n(l,t)$ can also be strongly varying over this interval when n is large because it contains quantities that depend on $2^n l$. For this reason the value of $f_n((l_i + \Delta l/2), t) c(2^n (l_i + \Delta l/2), 0)$ may not be a good approximation of $\langle f_n(l,t) c(2^n l, 0) \rangle_{l_i}$, necessitating the averaging. In computing the term $\langle f_n(l,t) c(2^n l, 0) \rangle_{l_i}$ by numerical summation the integration a step size of $\Delta l/2^n$ was employed.

6.3 End joining

For the case when end joining is included, a numerical integration procedure was used in which the $\langle c(l,t) \rangle_{l_i}$ at time $t = t_{j+1}$ are computed for the $\langle c(l,t) \rangle_{l_i}$ at time $t = t_j$ via the following update algorithm

$$\begin{aligned} \langle c(l, t_{j+1}) \rangle_{l_i} &= \sum_{n=0} \langle f_n(l, t_{j+1} - t_j) \langle c(2^n l, t_i) \rangle_l \rangle_{l_i} \\ &+ E_J(l_i, t_j)(t_{i+1} - t_i) \end{aligned} \tag{S51}$$

where $E_J(l_i, t_j)$ is

$$
\begin{aligned}
E_J(l, t) = & -\int_0^\infty dl' k(l, l') c(l, t) c(l', t) \\
& + \int_0^l dl' k(l', l - l') c(l', t) c(l - l', t)
\end{aligned}
\tag{S52}
$$

numerically evaluated for $l = l_i$ at $t = t_j$ using the $\langle c(l, t_j) \rangle_{l_i}$ for the $c(l, t)$.

6.4 Search algorithm

The unknown to be extracted from the data is the fragmentation volume function $V_f(l)$. A search algorithm was implemented that, under the constraints that $V_f(0) = 0$ and that $V_f(l)$ be a monotonically increasing function of l, sought to find a continuous piecewise linear function $V_f(l)$ that produced the best fit between the data and the numerical model. The function is specified by the values V_i of $V_f(l)$ at the tube length values l_i where the slope of $V_f(l)$ can change. The l_i were chosen according to:

$$
\begin{aligned}
l_0 &= 0, \\
l_1 &= 1/32, \\
l_2 &= 3/32, \\
l_3 &= 7/32, \\
l_4 &= 15/32 \\
l_i &= i - 4 - 1/32 \text{ for } i > 4.
\end{aligned}
\tag{S53}
$$

where the tube lengths l_i are in microns. The nonuniform distribution of the l_i for $i < 5$ was chosen to allow the investigation of $V_f(l)$ at the length scale of the smallest tube fragments observed. The initial V_i were chosen to be

$$
V_i = 0.01875i
\tag{S54}
$$

where the fragmentation volumes $V_i = V(l_i)$ are the fragmentation volumes in microliters (μl). The values of $V(l)$ for l not equal to one of the l_i were determined by linear interpolation between the l_i and l_{i+1} for which $l_i < l < l_{i+1}$.

The search algorithm proceeded by stochastically modifying the function $V_f(l)$ to produce the new function $V_f^{new}(l)$. The goodness of the fit of the model using $V_f^{new}(l)$ as the fragmentation volume was determined and compared with that of $V_f(l)$. If the fit using $V_f^{new}(l)$ was as good or better than that for $V_f(l)$, then V_f^{new} became the new $V_f(l)$. Otherwise $V_f^{new}(l)$ was discarded and $V_f(l)$ was retained as the fragmentation volume function. Each iteration of this process was counted as a generation. Good convergence of $V_f(l)$ to the optimum was obtained in 10,000 generations.

The procedure by which V_f^{new} is created is the following: An integer i_a with a uniform distribution on the interval $1 \le i_a \le 35$ was produced by a random number generator. A second random integer i_b with a uniform distribution on the interval $0 \le i_b \le 7$ was produced by a second random number generator. From these two random integers, two new random integers were created

$$
\begin{aligned}
i_1 &= i_a - i_b \\
i_2 &= i_a + i_b
\end{aligned}
\tag{S55}
$$

If i_1 was less than 1 it was reset to 1. If i_2 was greater than 35 it was reset to 35. Next, two random numbers r_1 and r_2 were generated from a random number generator which produced a uniform distribution between 0 and 1. If $i_2 < 35$ the $V_f^{new}(l_i)$ was created from $V_f(l_i)$ according to

$$
\begin{aligned}
V_f^{new}(l_i) = & \ V_f(l_i) + [V_f(l_{i_1-1}) - V_f(l_{i_1}))]r_1 \\
& + [V_f(l_{i_2+1}) - V_f(l_{i_2})]r_2
\end{aligned}
\tag{S56}
$$

for $l_{i_1} \le l_i \le l_{i_2}$ and

$$
V_f^{new}(l_i) = V_f(l_i)
\tag{S57}
$$

otherwise. If $i_2 = 35$ the $V_f^{new}(l_i)$ was created from $V_f(l_i)$ according to

$$V_f(l_i)^{new}(l) = V_f(l_i) + [V_f(l_{i_1-1}) - V_f(l_{i_1}))]r_1 + r_2 \tag{S58}$$

for $l_{i_1} \leq l_i$ and

$$V_f^{new}(l_i) = V_f(l_i) \tag{S59}$$

otherwise. This procedure randomly shifts a block, of variable width and position, of the function $V_f(l)$ up or down restricted to the maximum range allowed consistent with maintaining monotonicity. This procedure was adopted because the search algorithm was less susceptible to hang up at local optima than a procedure in which the $V_f(l_i)$ were individually updated.

In order to compare the model with the experiment, both the $c(l, t)$ measured experimentally and computed via the model were averaged over 1 μm intervals for successive intervals $l_i <= l < l_i + 1$ μm, where $l_{i+1} = l_i + 1$ starting with $l_0 = 0$. Let $\bar{c}(l_i, t_j)$ denote the experimental length distribution averaged over the ith interval and let $\bar{c}_m(l_i, t_j)$ denote the corresponding quantity calculated by the model. The quantity SD_1, consisting of the squared difference between $\bar{c}(l_i, t_j)$ and $\bar{c}_m(l_i, t_j)$ summed over all intervals i and and time points t_j at which the tube length distributions were measured, was used to compare the data with the model:

$$SD_1 = \sum_j \sum_i [\bar{c}(l_i, t_j) - \bar{c}_m(l_i, t_j)]^2. \tag{S60}$$

In addition, to assess the effectiveness of bursting bubbles in breaking short tubes the following averages were computed both for the experimental data and for the model

$$\bar{b}(\Delta_i, t_j) = \frac{1}{\Delta_i} \int_0^{\Delta_i} c(l, t_j)dl, \tag{S61}$$

where

$$\Delta_i = \frac{\Delta l}{2^i}. \tag{S62}$$

and $\Delta l = 1$ μm. That is, averages over the intervals with one end at the origin $l = 0$, were computed for 1/2, 1/4, 1/8, and 1/16 micron intervals. Let $\bar{b}(\Delta_i, t_j)$ denote these quantities computed for the experimental data and let $\bar{b}_m(\Delta_i, t_j)$ denote the corresponding quantities computed by the model. Then, the quantity SD_2, given by

$$SD_2 = \sum_j \sum_{i=1}^{4} [\bar{b}(\Delta_i, t_j) - \bar{b}_m(\Delta_i, t_j)]^2, \tag{S63}$$

was used to compare the data with the model for short tubes. The search algorithm sought to minimize the combined quantity

$$SD = SD_1 + W \cdot SD_2. \tag{S64}$$

where the weight W was taken to be 5×10^{-4}.

The statistical uncertainty in the determination of V_f, indicated in Fig. 5 was determined by generating new tube length lists from the experimentally obtained tube length lists via resampling using the withdraw from sample with replacement procedure (i.e. bootstrapping). These new tube length lists were binned to produce new $\bar{c}(l_i, t_j)$ distributions that were then processed using the procedures described above to extract the fragmentation volume functions for the resampled data. The mean, variance, and root-mean-square deviation (σ) of the bootstrapped ensemble of resulting fragmentation volumes were then computed. The "standard error of the mean" (S.E.M.) for the V_f parameter estimation is denoted by σ, as plotted in Fig. 5.

7 Derivation of the end-to-end joining rate constant

Here we derive Eq. (13) of the main text, the rate constant for the end-joining of two of our DNA nanotubes. For diffusion-controlled reactions, the rate constant for a second order reaction in which reactant 1 and reactant 2 are joined has the form

$$k_{12} = 4\pi(D_1 + D_2)L_{12} \tag{S65}$$

where D_1 and D_2 are the diffusion constants for reactant 1 and 2, respectively, and L_{12} is a characteristic distance that the reactants must approach each other in order to react [3].

In the present case the reactants are long rods whose reactive sites are at the ends of the rods. In this case both translational and rotational diffusion can be expected to play a role. However, in dilute solutions where the mean distance between the reactants is much larger than the length of the rods, translational diffusion will set the time scale on which the reactants find each other. Hence, D_1 and D_2 will be taken to be the translational diffusion constants for the rods. The diffusion constant D can be obtained from the rod mobility μ via the Einstein relation

$$D = \mu k_B T \tag{S66}$$

where k_B is Boltzmann's constant and T is the absolute temperature. Our rods are long compared to their radius ($R = 4$ nm). Hence, we have $R/l \ll 1$, where l is the rod length. To leading order in R/l, the mobility of a rod translated parallel to its long axis is (Ref. [4])

$$\mu_{||} = \frac{\ln(l/R)}{2\pi\eta l}, \tag{S67}$$

where η is the dynamic viscosity of the liquid. The mobility of the rod in a direction perpendicular to the long axis is half that of $\mu_{||}$:

$$\mu_T = \frac{1}{2}\mu_{||}. \tag{S68}$$

There are three independent directions of motion: one parallel, and two perpendicular to the long axis of the rod. Assuming that the orientation distribution of the rod is uniform due to rotational diffusion, the average mobility will be

$$\mu = \frac{2}{3}\mu_{||}. \tag{S69}$$

Hence, the translational diffusion constant for the rod is given by

$$D = \frac{k_B T \ln(l/R)}{3\pi\eta l}. \tag{S70}$$

Eq. (S65) can be written as

$$k_{12} = \frac{4 k_B T L_{12}}{3\eta R} \left(\frac{\ln(l_1/R)}{(l_1/R)} + \frac{\ln(l_2/R)}{(l_2/R)} \right). \tag{S71}$$

To determine the reaction's characteristic distance L_{12}, we first note that the DNA nanotubes have a polarity, such that the "+" end of one nanotube can only react with the "-" end of the other nanotube. We further assume that, because the single-stranded sticky ends are flexible, the two nanotubes do not need to be aligned with each other to initiate the joining reaction. Thus, for this purpose we treat the nanotubes as spherical reactants with radii R_1 and R_2, respectively, corresponding to the size of their reactive sites (but still with the diffusion constants D_1 and D_2 derived above). In this case, $L_{12} = R_1 + R_2$. The reactive sites of a rod consist of single-stranded DNA at each end that is able to hybridize with complementary single-stranded DNA on the other rods. These single-stranded DNA domains are 11 bases long (4.7 nm long). Adding this to the 4 nm radius of the rod suggests that the reactive ends can be treated approximately as spheres of radius $R_1 = R_2 = 9$ nm. Consequently, $L_{12} = 18$ nm. The resulting rate constant is likely an overestimate because of the spherical approximation we have made for the geometry of the reactive site and the assumption that a successful reaction occurs every time the reactive sites meet. We therefore introduce an effectiveness parameter $0 < \kappa < 1$. Finally, because both ends of each nanotube can react, we multiply by a factor of two, to arrive at the equation

$$k_{12} = \kappa \frac{12 k_B T}{\eta} \left(\frac{\ln(l_1/R)}{(l_1/R)} + \frac{\ln(l_2/R)}{(l_2/R)} \right). \tag{S72}$$

A similar equation for end-to-end joining of rod-like polymers was obtained by Hill [5]. Using our notation, and ignoring constants, his equation can be written as

$$k_{12} \sim \frac{1}{l_1 + l_2} \left(\frac{\ln(l_1)}{l_1} + \frac{\ln(l_2)}{l_2} \right). \tag{S73}$$

The difference between our results can be explained by Hill's assumption that the two rod-like polymers must be approximately aligned with each other in order to react, in contrast to our assumption that reactive ends can initiate successful binding regardless of their initial relative orientation. Again, our result is an overestimate.

Comparison to oligonucleotide hybridization suggests plausible ranges for the fraction of effective collisions, κ. Approximating oligonucleotides of length N nucleotides as spheres of radius $R_1 = R_2 = R_s = \sqrt{N} \times 0.43$ nm, we follow the analysis of Calef and Deutch [3] and use $D_1 = D_2 = D_s = k_B T/6\pi\eta R_s$ and

$$k_{12} = \kappa \ 4\pi(D_1 + D_2)(R_1 + R_2) = \kappa \frac{8k_B T}{3\eta}, \tag{S74}$$

where we have added κ to account for ineffective collisions. Interestingly, this estimate is independent of R_s and thus N; however, we might expect that κ has a dependence upon N. Here we will extract κ from measurements of the rate constant for hybridization of two 10-mers, which was found to be $\sim 1.0 \times 10^7$ /M/s at 30 °C in a 1 M Na$^+$ buffer [6]. Thus, we have

$$k_{12} = \kappa \times 6.6 \times 10^9 \ /\text{M/s} \sim 1.0 \times 10^7 \ /\text{M/s} \tag{S75}$$

and thus $\kappa \sim 1.5 \times 10^{-3}$ for 10-mer hybridization, i.e. roughly only 1 in 660 collisions leads to duplex formation. In the case of end-to-end joining of 7-helix DNA nanotubes, each end has 7 length-10 or length-11 sticky ends with distinct sequences (Fig. S1). Presuming that each collision has a 1-in-7 chance of allowing interaction between complementary sticky ends, and presuming that 1 in 660 of such collisions leads to successful end-to-end joining of the nanotubes, we obtain $\kappa_{ref} = 2.2 \times 10^{-4}$. However, because of the slower translational diffusion in nanotubes relative to oligonucleotides, the attempt frequency and success probability could be larger than the estimate provided here, necessitating experimental assessment. In the main text, we note that poorer fits to our experimental data result when larger values of κ are used, providing some evidence in support of our suggested reference value of κ. Here, we also note that even if κ were as large as $122 \times \kappa_{ref}$, the inferred fragmentation volumes remain within a factor of 10 of those reported in Fig. 5.

8 Angular deviation of a rod from the elongation axis due to Brownian motion

Although a rod shaped object subjected to elongation flow is expected to orient along the direction of elongation, Brownian fluctuation however, acts to misalign the rod through rotational diffusion. This diffusion rate is greater for smaller objects and may reduce how effectively elongation flow can shear nanorods. Here we compute the mean-square-angular deviation of the rod axis from the axis of elongation for a rod subjected to pure elongation flow and show that this deviation is equal to the Péclet number for a suitable choice of characteristic velocity and characteristic length.

For the analysis, we consider the case when the tube is much longer than its radius, so that terms need be kept only to leading order in l/R, where l is the tube length and R is the tube radius. We also use the small angle approximation $\sin(\theta) \approx \theta$, where θ is the angle of misalignment of the tube from the axis of elongation. This axis is taken to lie along the z axis. In the main text, we show that our experimental conditions warrant these approximations.

Consider pure elongation flow, with axis of elongation oriented along the z axis, and with stagnation point at the origin. The radial, ϕ and z components of the velocity field are given by

$$\begin{pmatrix} u_r \\ u_\phi \\ u_z \end{pmatrix} = \begin{pmatrix} -\dot{\epsilon}r/2 \\ 0 \\ \dot{\epsilon}z \end{pmatrix}. \tag{S76}$$

The stress on a surface element of the rod along the axis of elongation [7] is given by

$$\sigma_{rz} = \frac{\eta\dot{\epsilon}z}{R\ln(l/2R)}. \tag{S77}$$

If the rod is misaligned from the z axis by a small angle θ, it will experience a restoring torque given by

$$T_r = 4\pi R \int_{-l/2}^{l/2} \sigma_{rz}z\theta dz = \frac{\pi\eta\dot{\epsilon}l^3\theta}{3\ln(l/2R)}, \tag{S78}$$

where the rod's center has been chosen to be at the stagnation point.

A torque will also be generated as the rod is rotated in the fluid due to opposing forces generated by the fluid viscosity. This torque is given by

$$T_\eta = \eta_R \frac{d\theta}{dt}, \tag{S79}$$

where the torque constant is given by

$$\eta_R = \frac{\pi \eta l^3}{3 \ln(l/R)}. \tag{S80}$$

See for example J. Riseman and J. G. Kirkwood [4], or S. Broersma [8]. Associated with this frictional torque is a fluctuating torque T_n that has zero mean and whose two time correlation function is given by

$$\langle T_n(t) T_n(t') \rangle = 2\eta_R k_B T \delta(t - t'). \tag{S81}$$

This torque induces Brownian motion with a rotatory diffusion constant given by

$$D_r = \frac{k_B T}{\eta_R}. \tag{S82}$$

See for example D. A. Tsyboulski, *et al.* [9].

Torque balance requires

$$T_\eta + T_r = T_n. \tag{S83}$$

Substituting Eqs. (S78) and (S79) into this equation and using approximation $\ln(l/2R) \sim \ln(l/R)$, since we are considering the case when $l \gg R$, reduces this equation to the Langevin equation

$$\frac{d\theta}{dt} + \dot{\epsilon}\theta = \frac{T_n}{\eta_R}. \tag{S84}$$

To determine the mean-square deviation of θ from zero due to Brownian fluctuations, it is convenient to convert this differential equation into the integral equation

$$\theta = \frac{1}{\eta_R} \int_{-\infty}^{t} e^{-\dot{\epsilon}(t-t')} T_n(t') dt. \tag{S85}$$

It is then straightforward to show that

$$\langle \theta^2 \rangle = \frac{k_B T}{\eta_R \dot{\epsilon}} = \frac{3 k_B T \ln(l/R)}{\pi \eta \dot{\epsilon} l^3}. \tag{S86}$$

.

Following M. Manhart [10], we introduce the Péclet number

$$\text{Pe} = \frac{\partial u_z / \partial z}{D_r} = \frac{\dot{\epsilon}}{D_r}. \tag{S87}$$

Using Eqs. (S76) and (S82), and comparing to Eq. (S86) one finds

$$\langle \theta^2 \rangle = \frac{1}{\text{Pe}}. \tag{S88}$$

## 9 Analysis of the fragmentation of tube-like multilamellar vesicles

Here we estimate the elongation rate that is required to fragment, to 1 μm lengths, the tubular multilamellar vesicles whose fragmentation Zhu and Szostak [11] have studied as a possible means by which protobionts may have carried out cell division.

In a typical experiment, the vesicle starts out as a sphere having a radius of 2 μm. The initial volume of the vesicle is 33.5 μm^3 and it initial area is 25.1 μm^2. Upon incorporating micelles into the vesicle, the vesicle

increases its area 3.7 fold. Due to the impermeability of the wall, the volume remains fixed. To accommodate the increased area while keeping the volume fixed the vesicle adopts a branched filament configuration where the filaments have a radius r of 0.18 μm and the total length of the filaments is 81 μm. When these filaments are sheared by fluid flow they reform spherical vesicles without spilling their contents into the surrounding medium. It is this latter property that makes the fragmentation of these filaments attractive as a primitive form of cell division.

Although Zhu and Szostak showed that this mechanism operates for vesicles made from a variety of lipids, the one that received the most study was olic acid. This molecule is 2.06 nm long. The bilayer lamella has a thickness that is twice this, namely $t = 4.12$ nm. The cross-sectional area presented by the lamella is thus $A_l = 2\pi r t$ or 4.6×10^{-3} μm^2. To estimate the tensile force required to shear a vesicle with a lamella of this cross-section we will assume that the tensile strength of of an olic acid lamella is the same as that of paraffin wax, since the two consist of linear chains of mostly saturated hydrocarbon. The tensile strength σ_T of paraffin wax is roughly 1 MPa [12]. The tensile force required to shear the vesicle is thus $T = \sigma_t A_l = 4.6$ nN. Using this number, $l = 1$ μm, and $R = r$ in Eq. (1) of the main text one finds $\dot{\epsilon} = 2.5 \times 10^6$ sec^{-1}. This is the elongation rate required to fragment the tube like vesicle into fragments 1 μm long. For a multilamellar vesicle, consisting of n lamellar layers, the elongation rate required for fragmentation becomes $\dot{\epsilon} = 2.5 \times 10^6$ sec$^{-1} \times n$.

10   Supplementary Movie
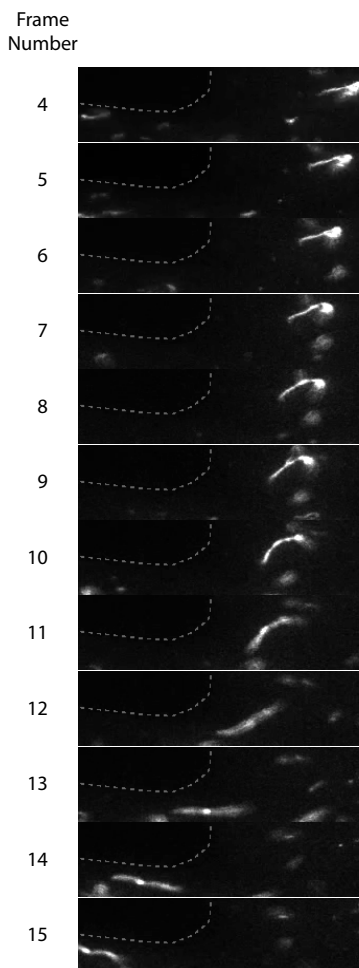
Movie S1. Fluorescence movie (1 frame/sec) of Cy3-labeled DNA nanotubes in a microfluidic channel (dashed lines, height 100 μm) under slow flow rate (right to left, 47 μm/sec in the center). The nanotubes experienced compressional and elongational flows as they enter and exit the side chamber, respectively. The maximum elon-

gational flow in the channel was estimated to be 1.4 /sec, which is, using a conformational relaxation time of 400 ms for the nanotubes, within a factor of two of the critical threshold for polymer stretching [13]. The measured maximum elongational flow during the bursting of a bubble (Fig. S1) is $\sim 10^8$-fold larger than in the channel. Consequently, the elongational flow during the expansion of the bubble hole is expected to orient and stretch DNA nanotubes. Given the longest observed nanotube in the movie is 52 μm, the maximum elongational-flow-induced tension in the channel was calculated to be 1.2 pN (Eq. 1). The maximum generated tension in the movie is more than two-orders of magnitude smaller than the critical tension to break a 7-helix DNA nanotubes (455 pN). The weak hydrodynamic-induced tension is sufficient to explain the absence of nanotube scission in the movie.

References

[1] Yin P, et al. (2008) Programming DNA tube circumferences. *Science* 321:824–826.

[2] Schiffels D, Liedl T, Fygenson DK (2013) Nanoscale structure and microscale stiffness of DNA nanotubes. *ACS nano* 7:6700–6710.

[3] Calef DF, Deutch J (1983) Diffusion-controlled reactions. *Annual Review of Physical Chemistry* 34:493–524.

[4] Riseman J, Kirkwood JG (1950) The intrinsic viscosity, translational and rotatory diffusion constants of rod-like macromolecules in solution. *The Journal of Chemical Physics* 18:512–516.

[5] Hill TL (1983) Length dependence of rate constants for end-to-end association and dissociation of equilibrium linear aggregates. *Biophysical journal* 44:285–288.

[6] Morrison LE, Stols LM (1993) Sensitive fluorescence-based thermodynamic and kinetic measurements of DNA hybridization in solution. *Biochemistry* 32:3095–3104.

[7] Hariadi RF, Yurke B (2010) Elongational-flow-induced scission of DNA nanotubes in laminar flow. *Physical Review E* 82:046307.

[8] Broersma S (1960) Rotational diffusion constant of a cylindrical particle. *The Journal of Chemical Physics* 32:1626–1631.

[9] Tsyboulski DA, Bachilo SM, Kolomeisky AB, Weisman RB (2008) Translational and rotational dynamics of individual single-walled carbon nanotubes in aqueous suspension. *ACS Nano* 2:1770–1776.

[10] Manhart M (2004) Visco-elastic behaviour of suspensions of rigid-rod like particles in turbulent channel flow. *Eur J of Mec B-Fluid* 23:461 − 474.

[11] Zhu TF, Szostak JW (2009) Coupled growth and division of model protocell membranes. *Journal of the American Chemical Society* 131:5705–5713.

[12] DeSain JD, Brady BB, Metzler KM, Curtiss TJ, Albright TV (2009) Tensile tests of paraffin wax for hybrid rocket fuel grains. *AIAA* 5115:1–27.

[13] Smith DE, Chu S (1998) Response of flexible polymers to a sudden elongational flow. *Science* 281:1335–1340.